Zitierweise: *Angew. Chem. Int. Ed.* **2023**, *62*, e202305944
doi.org/10.1002/anie.202305944

VIP Gas Separation Very Important Paper

Induced-Fit-Identification in a Rigid Metal-Organic Framework for ppm-Level CO_2 Removal and Ultra-Pure CO Enrichment

Peng Hu, Jialang Hu, Min Zhu, Chao Xiong, Rajamani Krishna, Dan Zhao, and Hongbing Ji**

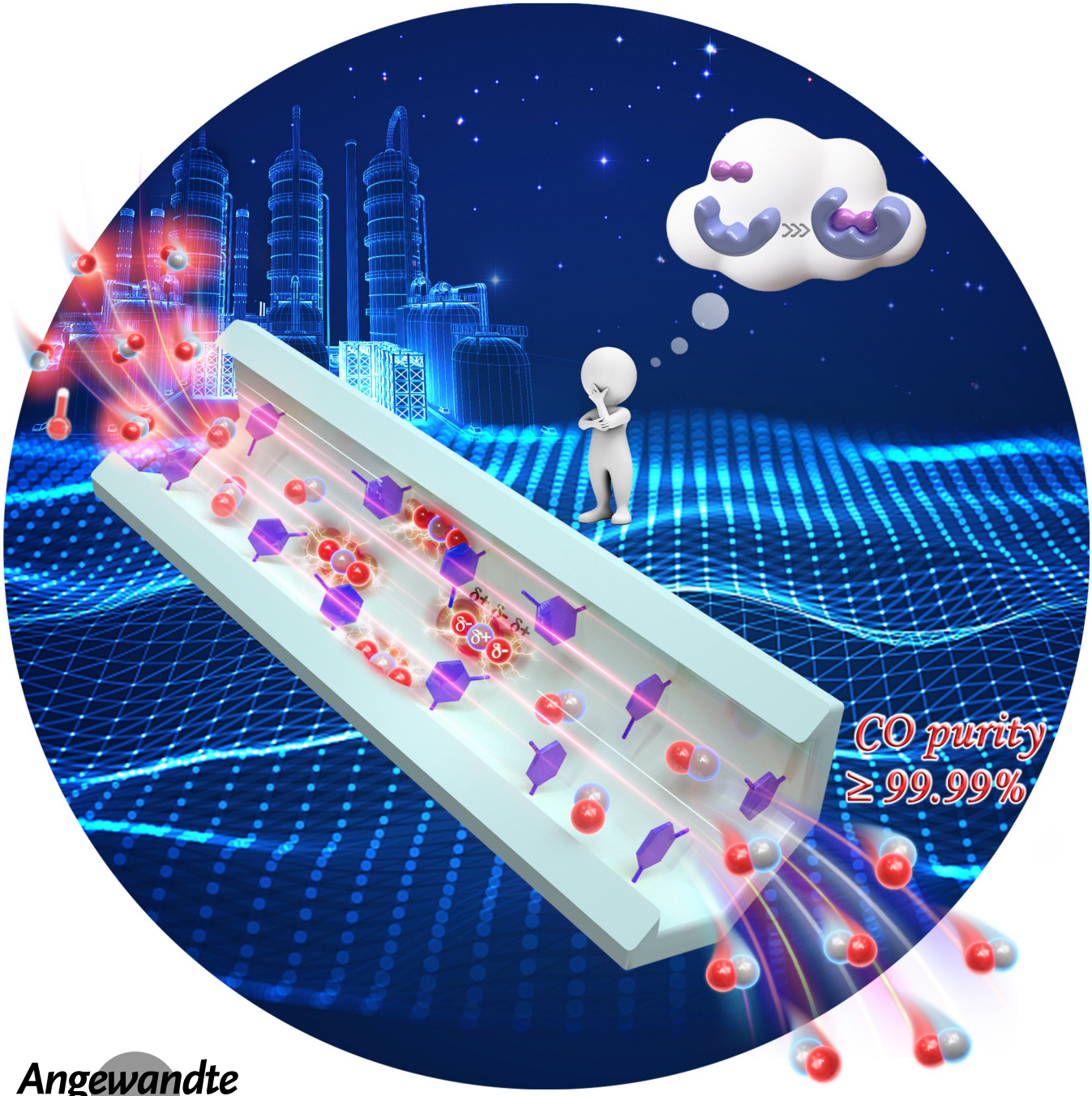

Abstract: Removing CO_2 from crude syngas via physical adsorption is an effective method to yield eligible syngas. However, the bottleneck in trapping ppm-level CO_2 and improving CO purity at higher working temperatures are major challenges. Here we report a thermoresponsive metal–organic framework (**1a-apz**), assembled by rigid Mg_2(dobdc) (**1a**) and aminopyrazine (apz), which not only affords an ultra-high CO_2 capacity (145.0/197.6 $cm^3 g^{-1}$ (0.01/0.1 bar) at 298 K) but also produces ultra-pure CO (purity $\geq$99.99 %) at a practical ambient temperature (T_A). Several characterization results, including variable-temperature tests, in situ high-resolution synchrotron X-ray diffraction (HR-SXRD), and simulations, explicitly unravel that the excellent property is attributed to the induced-fit-identification in **1a-apz** that comprises self-adaption of apz, multiple binding sites, and complementary electrostatic potential (ESP). Breakthrough tests suggest that **1a-apz** can remove CO_2 from 1/99 CO_2/CO mixtures at practical 348 K, yielding 70.5 $L kg^{-1}$ of CO with ultra-high purity of $\geq$99.99 %. The excellent separation performance is also revealed by separating crude syngas that contains quinary mixtures of $H_2/N_2/CH_4/CO/CO_2$ (46/18.3/2.4/32.3/1, v/v/v/v/v).

Introduction

Direct conversion of syngas-to-light olefins (STO) is a promising approach to alleviate the overdependence on petroleum resources.[1] Syngas production through dry reforming of methane (DRM) has been an emerging method to utilize CO_2 and CH_4 as feedstocks to make syngas while mitigating both greenhouse gases.[2] In industrial scenarios, crude syngas produced by DRM needs multi-step separations to obtain eligible CO and H_2 with high purity required by STO.[3] CO_2, the inevitable impurity that usually exists in CO feed gas due to their similar molecule sizes (CO_2: 3.3 Å; CO: 3.76 Å),[4] not only reduces the quality of CO but also corrodes pipelines in the presence of moisture.[5] Therefore, effectively removing the CO_2 impurity from CO feed gas is an imperative prerequisite.[6] Currently, CO_2 removal through cryogenic distillation or aqueous ammonia absorption are well-known processes, yet suffering the limitations of high energy consumption, environmental pollution, and the inability to achieve pure CO ($\geq$99.5 %).[3,7] Adsorptive removal of the low-concentration CO_2 impurity from CO_2/CO mixtures or even from quinary crude syngas (typically consisting of ca. 46 % H_2, 18.3 % N_2, 2.4 % CH_4, 32.3 % CO, and 1 % CO_2)[7] is urgently needed but challenging.

Over the past several years, metal–organic frameworks (MOFs)[8] have been developed for CO purification, given their diverse virtues.[3–4,9] However, the unqualified CO purity and reduced productivity at a meaningful temperature impede their applications because crude CO feed usually requires being maintained at higher T_A to ensure its vapor phase.[3,10] Currently, two MOFs with thermoresponsive behaviors have been reported for C_3H_6/C_3H_8 separation.[10–11] However, their frameworks are flexible and require sufficient pressure to surpass the threshold for breathing behavior,[12] which are unsuited for trace CO_2 removal. Previously, we reported pz-functionalized (pz = pyrazine) Co-MOF, a typical rigid candidate, that showed excellent trace CO_2 capture.[13] Such a discovery enlightens us to investigate its derivatives with thermoresponsive nature for trace CO_2 removal under realistic T_A.

Herein, we target a rigid MOF with a thermoresponsive nature, exhibiting enhanced CO_2 capacity under practical T_A through a unique induced-fit-identification (Scheme 1). Detailedly, Mg_2(dobdc) (**1a**, aka Mg-MOF-74[14]) was selected as the rigid platform to assemble a thermoresponsive MOF (**1a-apz**). Theoretical analysis reveals its augmented pore access of apz-functionalized **1a** in response to thermal stimulus, accompanied by electrostatic potential reconfiguration (Figure 1). Gas adsorption tests suggest an ultra-high CO_2 capacity of 145.0/197.6 $cm^3 g^{-1}$ (0.01/0.1 bar) for **1a-apz** at 298 K. Breakthrough tests reveal that **1a-apz** can recover trace CO_2 from 1/99 CO_2/CO, yielding a higher CO productivity of 70.5 $L kg^{-1}$ with ultrahigh purity of $\geq$99.99 % at 348 K and 1 bar. Variable-temperature tests, CO_2-loaded in situ experiments, in situ HR-SXRD, and simulations jointly reveal that an unusual induced-fit-identification can be initiated for ppm-level CO_2 removal and ultra-pure CO enrichment in response to the threshold temperature. Breakthrough tests using quinary crude syngas containing $H_2/N_2/CH_4/CO/CO_2$ (46/18.3/2.4/32.3/1, v/v/v/v/v) also confirm its great potential in separating CO_2 (1 %) from multiple components under realistic temperature.

[*] Dr. P. Hu, J. Hu, Dr. C. Xiong, Prof. H. Ji
Fine Chemical Industry Research Institute,
School of Chemistry,
Sun Yat-Sen University
510275 Guangzhou, (P. R. China)
E-mail: jihb@mail.sysu.edu.cn
Dr. P. Hu, Prof. D. Zhao
Department of Chemical and Biomolecular Engineering,
National University of Singapore
4 Engineering Drive 4, 117585 Singapore (Singapore)
E-mail: chezhao@nus.edu.sg
Dr. M. Zhu
MOE Laboratory of Bioinorganic and Synthetic Chemistry,
School of Chemistry,
Sun Yat-Sen University
510275 Guangzhou, (P. R. China)
Prof. R. Krishna
Van't Hoff Institute for Molecular Sciences,
University of Amsterdam
Science Park 904, 1098 XH Amsterdam (The Netherlands)
Prof. H. Ji
State Key Laboratory Breeding Base of Green-Chemical Synthesis Technology,
Institute of Green Petroleum Processing and Light Hydrocarbon Conversion,
College of Chemical Engineering,
Zhejiang University of Technology
310014 Hangzhou, (P. R. China)

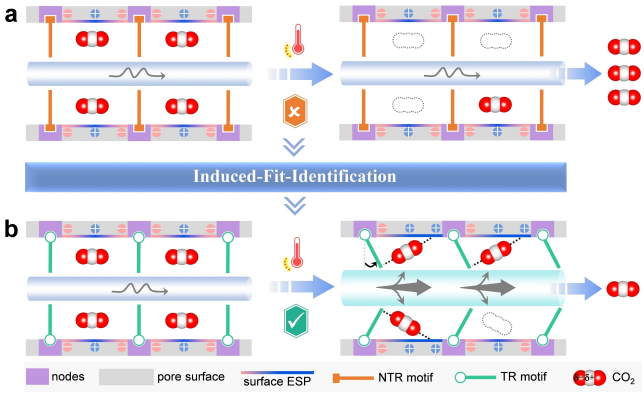

Scheme 1. Schematic illustration of the induced-fit-identification mechanism for CO_2 capture under practical conditions with higher T_A. (a) For CO_2 adsorbed in most rigid MOFs, the working conditions with higher T_A usually result in a significant reduction in CO_2 capacity due to the exothermic physical process. (b) A sensitive motif can be judiciously assembled into the rigid MOF to endow the rigid MOF with thermoresponsive character and fast diffusion behavior, thus contributing to enhanced CO_2 capacity through thermoregulatory self-adaption, multiple sites, and unusual complementary ESP effects (NTR: non-thermoregulatory; TR: thermoregulatory).

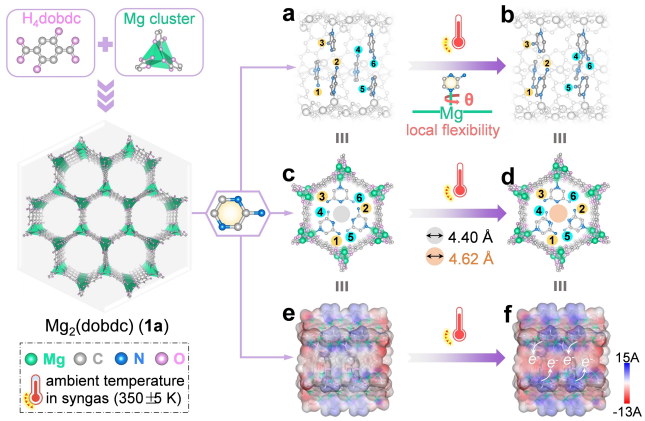

Figure 1. Topological diagrams of apz functionalized **1a-apz**. (a–b) Spatial configurations of apz motif in **1a-apz** along the crystallographic *a*-axis; (c–d) Static pore conformation of **1a-apz** along the crystallographic *c*-axis; (e–f) The ESP of **1a-apz** mapped onto the Connolly surface. The gradation on the scale bar is in kcal mol^{-1}.

Results and Discussion

1a hexahedron nanocrystal (Figure S1a–b) and **1a** derivatives (denoted as **1a-pz** and **1a-apz**) were prepared through our reported method with modifications.[13] By comparing theoretical and powder X-ray diffraction (PXRD) patterns (Figure S2), all samples exhibit consistency and crystallize in the hexagonal system with $R\bar{3}c$ space group. Thermogravimetric analyses suggest increased thermal stability after introducing pz and apz entities, yielding improved decomposition temperatures of ca. 350 °C for **1a-pz** and 426 °C for **1a-apz** (Figure S3). Further, the ^{1}H nuclear magnetic resonance (^{1}H NMR) analyses were performed to quantify the actual content of pz derivatives in **1a**. As shown in Figure S4–5, the ratios of H in dobdc^{4-} to that in the pz and the benzene ring of apz groups were quantified to be 0.49 and 0.66, respectively (excluding the H atom attached to the amino group of apz), which are close to the theoretical values of 0.5 and 0.67 calculated from given formula units ([Mg_2(dobdc)(pz)]) or ([Mg_2(dobdc)(apz)]). The consistency can be evidenced by elemental analysis (EA) and inductively coupled plasma optical emission spectroscopy (ICP-OES). As shown in Table S1, the experimental molar ratios of elements in **1a-pz** and **1a-apz** were almost equal to the theoretical values. The results indicate that one pz or apz molecule can be successfully bonded to the formula unit ([Mg_2(dobdc)(pz)]) for **1a-pz** or ([Mg_2(dobdc)(apz)]) for **1a-apz**.

Single crystals of **1a-pz** and **1a-apz** were attempted but failed. Instead, HR-SXRD (Figure S6) was conducted on **1a-pz** and **1a-apz**, striving to determine the spatial position of pz and apz. The collected HR-SXRD patterns of **1a-pz** and **1a-apz** agree well with the theoretical ones (Figure S7a–b). Rietveld refinements on HR-SXRD data were performed, yielding an $R\bar{3}c$ space group and crystallographic parameters with satisfied R_p and R_{wp} factors for **1a-pz** and **1a-apz** (Figure S7c–d and Table S2). Based on the refined structures, pz and apz motifs in **1a** adopt periodic binding configurations (Figure S8a–c, S8d–f) and display the perpendicular plane conformation to the crystallographic *c*-axis (Figure S8c, S8f). In particular, for **1a-apz**, the spatial orientation of NH_2 adopts a staggered arrangement in the channel (Figure S8d–f). The geometrical arrangement of pz and apz along the crystallographic *c*-axis could be visually reflected on the two-dimensional electron-density maps (2D-EDM) of **1a-pz** and **1a-apz**. As shown in Figure S9a–b, the electron density diffraction projected by pz motifs on the lattice plane with the Miller indices of (100) is evident, and adjacent diffraction spots of pz show nearly parallel queues along the *c*-axis. Similarly, the above results could also be observed through 2D-EDM of apz in **1a-apz** structure (Figure S9c–d).

Given the above analysis, we thus modeled MOF structures using well-versed molecular dynamics (MD) combined with density functional theory (DFT). As revealed in Figure S10–11, the optimized topology structures with the lowest steady-state energy (19.8 kJ mol^{-1} for **1a-pz** and 28.3 kJ mol^{-1} for **1a-apz**) were used as the initial models for further analysis. Besides, the bonding distances of N–Mg bonds and non-bonding distances, including pyridine N···N types along the *c*-axis or amino N···N types along the *a*-axis, were compared. As shown in Figure S12–13 and Table S3–4, the relative errors between experimental and theoretical results for the same bonding configurations are 0.41–5.24 % for **1a-pz** and 0.46–6.64 % for **1a-apz**, suggesting reasonable theoretical models.

N_2 sorption tests at 77 K were performed to probe the porosity. As seen in Figure S14a, the N_2 uptake capacity of all the materials can quickly reach equilibrium under lower pressures, yielding microporous Type-I adsorption isotherms. Brunauer–Emmett–Teller (BET) surface areas follow the hierarchy of **1a** (1300 m^2 g^{-1}) > **1a-pz** (1006 m^2 g^{-1}) > **1a-apz** (877 m^2 g^{-1}), and pore size distribution

(PSD) data suggest a uniform aperture distribution of ca. 8.7 Å for **1a**, yet reduced PSD for **1a-pz** (5.8 Å) and **1a-apz** (4.4 Å) (Figure S14b). The eternal pore attributes prompted us to evaluate the static adsorption performance of CO and CO_2. As shown in Figure S15a, **1a-apz** exhibits an excellent adsorption capacity of 121.2 $cm^3 g^{-1}$ for CO at 298 K and 1 bar, higher than that of **1a** (73.8 $cm^3 g^{-1}$) and **1a-pz** (87.0 $cm^3 g^{-1}$). Concerning CO_2, the materials demonstrate impressive adsorption behaviors under lower CO_2 concentrations, as indicated by the remarkable steepness of CO_2 isotherms (Figure 2a). Especially for **1a-apz**, ultrahigh CO_2 capacity is visible under low concentrations of 1000 ppm to 0.1 bar (10^5 ppm), giving the ultrahigh CO_2 uptakes of 54.9/145.0/197.6 $cm^3 g^{-1}$ (10^3/10^4/10^5 ppm) at 298 K. Further comparisons of CO_2 capacity indicate that **1a-apz** surpasses all the cutting-edge materials (Figure 2b), including Zu-16-Co (58.9/62.7 $cm^3 g^{-1}$),[15] Co-MOF (28.7/89.7 $cm^3 g^{-1}$),[13] and TIFSIX-3-Ni (44.8/47.0 $cm^3 g^{-1}$)[16] at 0.01/0.1 bar and 298 K, suggestive of gratifying prospect in trapping trace CO_2.

We further collected isotherms at higher temperatures, given that the feed gases are practically maintained at sufficient T_A to ensure their vapor-phase state before flowing into the separation unit.[10] As illustrated in Figure 2c and Figure S15b–c, the sorption isotherms of CO_2 on the three samples exhibit a common decrease as T_A increases. Closer inspection, however, reveals an atypical phenomenon for **1a-apz** as T_A increases to 348 K. Specifically, the CO_2 uptake difference between 328 and 348 K (denoted as ΔQ3) exhibits a reduced preference compared to that between 298 and 313 K (denoted as ΔQ1) or between 313 and 328 K (denoted as ΔQ2) (Figure 2c) at 0.01 bar. Similarly, it also displays decreased ΔQ6 compared to ΔQ4 and ΔQ5 at 0.1 bar. Adsorption isotherms suggest that the abnormal character can still be observed at 358 K, and the capacity declines sharply when the temperature increases to 368 K (Figure S15d). Such atypical sorption behavior on **1a-apz** was not observed for CO (Figure S16a). Further, the calculated uptake ratios of CO_2/CO per unit cell give the highest value of 4.46 at 348 K and 0.1 bar (Figure S16b), revealing its outstanding potential in capturing CO_2 under high T_A. Notably, the CO_2 isotherms in this study differ from the step-shaped adsorption isotherms frequently observed on mmen-M_2-(dobpdc) due to chemisorption,[17] which has high CO_2 adsorption heat exceeding 60 kJ mol^{-1}. The coverage-dependent adsorption heats of **1a-apz** obtained by the virial method (Table S5) were calculated to be 48.9 kJ mol^{-1} for CO_2 and 25.2 kJ mol^{-1} for CO (Figure S17), suggestive of typical physisorption processes.

To deeply understand the abnormal adsorption behavior, we collected variable-temperature-dependent PXRD patterns (VT-PXRD). As shown in Figure 2d, the diffraction peaks corresponding to (110) planes demonstrate no shifts as temperature increases from 298 K to 328 K. However, they begin to shift to lower 2θ angles at 348 K or 358 K due to structural fluctuation or flexibility of apz motif in **1a-apz**, resulting in enhanced *d*-spacing in **1a-apz**. Derived top contour plots of VT-PXRD patterns (Figure 2e) evidence that the main peaks associated with (110) and (300) planes remain unconstant at all temperatures, excluding the presence of thermal-induced phase transformation. To under-

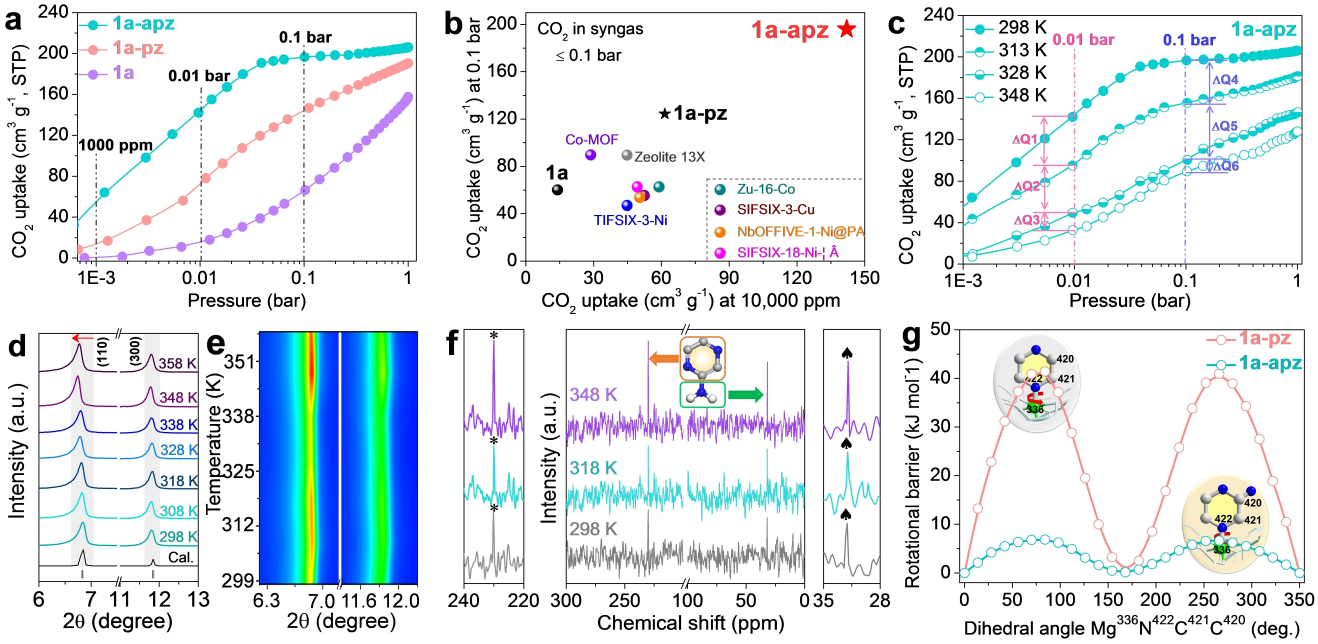

Figure 2. (a) Adsorption isotherms of CO_2 on the activated samples at 298 K and 1 bar; (b) Comparisons of CO_2 uptake with low pressures of 0.1 bar and 10,000 ppm at 298 K on some chosen materials; (c) Adsorption isotherms of CO_2 on **1a-apz** under variable temperatures at 1 bar; (d) Variable-temperature PXRD patterns for **1a-apz** under air atmosphere in the temperature range from 298 to 358 K and (e) its two-dimensional contour plots as a function of 2θ and temperature, indicating preferable structural rigidity; (f) The CPMAS ^{15}N solid-state NMR spectra of the isotopically labeled **1a-apz** at different temperatures; (g) The variation of the total energy as the pz or apz rotated around Mg^{336}–N^{422} bonding, derived from DFT calculations.

stand such flexible behavior thoroughly, we used ^{15}N solid-state NMR to explore the linker rotational dynamics at variable temperatures. From the CPMAS ^{15}N solid-state NMR spectra of isotopically labeled **1a-apz** (Figure 2f), we observed that the signals of amino-N and pyridine-N concentrated at 28–35 ppm[18] and 220–240 ppm[19] displayed a quasi-unchanged intensity in resolution as T_A rose from 298 to 318 K, yet a reversed increase as T_A continued to increase to 348 K. Similar trends for pyridine-N were not found in **1a-pz** (Figure S18a), suggesting that amino-N and pyridine-N in **1a-apz** have undergone thermoresponsive motion at 348 K.[20] In situ variable-temperature-dependent Raman results suggest that the vibration character of apz moiety located at 649 cm^{-1} migrates from 650 cm^{-1} to 635 cm^{-1} as T_A increases from 318 K to 348 K (Figure S18b), ascribing to the rotational dynamic attribute of apz in **1a-apz**.[21] To further investigate the rotational barrier of pz and apz at the molecular level, we performed quantum chemistry with *Gaussian* 09 software.[22] As illustrated in Figure 2g, the dihedral angle with atomic configurations of $Mg^{336}N^{422}C^{421}C^{420}$ in **1a-apz** exhibits ultra-low rotation and flipping energies of only 6.7 kJ mol^{-1}, which is much lower than that of **1a-pz** (41.3 kJ mol^{-1}). Thus, the adsorption heat of CO_2 will effortlessly overcome the energy required for apz rotation. Meanwhile, molecular simulations were investigated to compare the steady-state geometry conformation with lowest energies at 298 and 348 K. As clearly observed in Figure S19a, two host frameworks of **1a-apz** exhibit quasi-accordant conformation overlap, yet the dangling apz motifs in the same spatial location adopt staggered conformations (denoted as **I**, **II** and **III**, inset in Figure S19a). Taking **Scenario I** as an example, the spatial staggered conformation of two apz molecules is amplified and displayed in geometrical plane views. As shown in Figure S19b, two apz molecules of **1a-apz** in the same position reveal different planar orientations from a static view, yielding a dihedral angle of 36.1°. Likewise, for apz located at **Scenario II** and **III**, the staggered geometrical planes also exhibit dihedral angles of 28.7° for **Scenario II** (Figure S19c) and 30.0° for **Scenario III** (Figure S19d). Obviously, the different planar orientations at 298 K and 348 K further confirm the dynamic flexibility of apz, expecting to engineer the pore microenvironment of **1a-apz**.

Further, CO_2-loaded in situ Raman coupled with in situ FT-IR tests were conducted to elucidate the potential binding mechanism. As demonstrated by the CO_2-loaded in situ Raman results (Figure 3a), the peak located at 568.9 cm^{-1} is ascribed to Mg–O stretching modes in **1a-apz** clusters. The C–H bending of benzene ring, C=O, and O–C–O symmetric stretching of the carboxylate group in $dobdc^{4-}$ are reflected by the signals at 819.4, 1290.8, and 1422.9 cm^{-1}, respectively.[23] Notably, the peak strength of N–C(CO_2) bonding at 732.9 cm^{-1} remains unchanged with increasing temperature (Figure 3a), indicating that the binding interaction between CO_2 and **1a-apz** is undisturbed in response to an ambient thermal stimulus. Besides, emerging

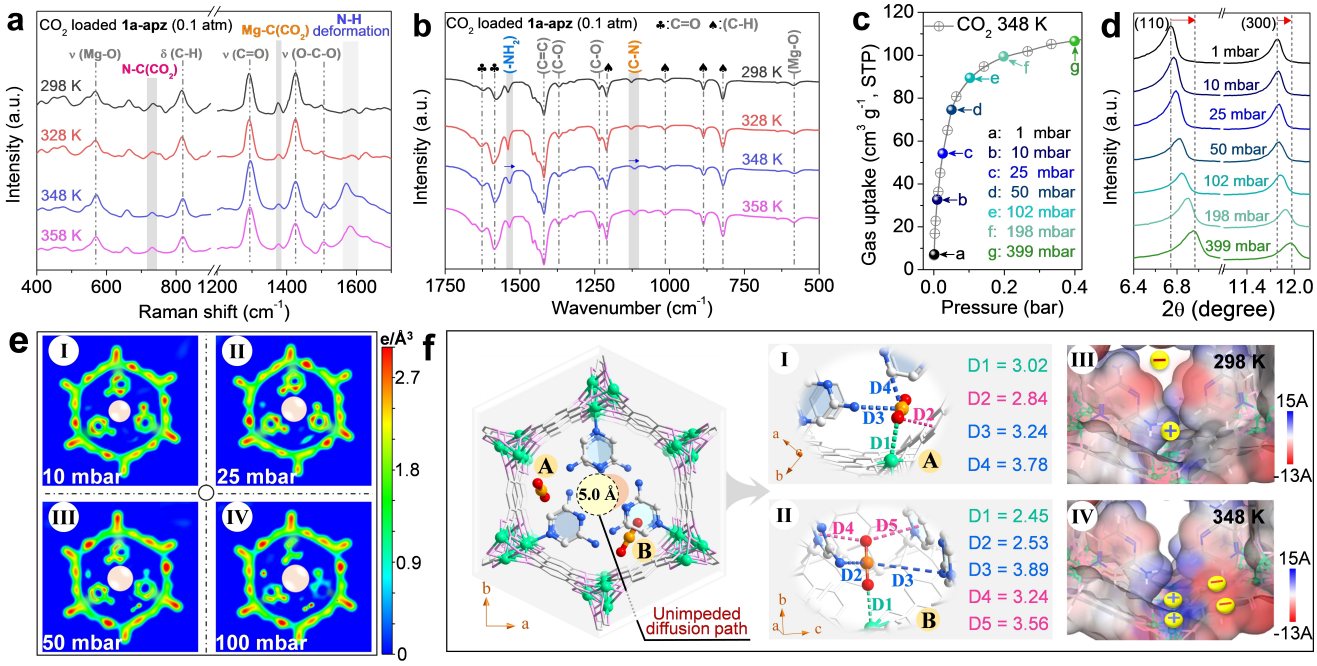

Figure 3. (a) In situ variable-temperature Raman and (b) FT-IR of CO_2-loaded **1a-apz**; (c) CO_2 adsorption isotherm of **1a-apz** at 348 K and (d) corresponding PXRD patterns of CO_2⊂**1a-apz** measured at each point shown in the CO_2 adsorption isotherm; (e) Intuitional 2D-EDM yielded from experimental PXRD of CO_2-loaded **1a-apz**, with 10, 25, 50, and 100 mbar of saturated CO_2 pressure, respectively; (f) DFT calculated adsorption conformation of CO_2-loaded **1a-apz** at 348 K and ESP of **1a-apz** mapped onto the Connolly surface (The binding types colored with green, blue, and pink correspond to the π-complexation effect, Lewis acid/base interactions, and van der Waals interaction, respectively. Here the bond lengths are in angstroms. Color modes: Mg, green; O, light pink; N, blue; C, gray-25%; H atoms were omitted for clarity. The gradation on the scale bar in ESP is in kcal mol^{-1}).

N–H deformation vibration at 1570.8 cm^{-1} at 348 K confirms the thermal-sensitive local flexibility of apz,[24] which can exert synergetic effects on CO_2 capture. In addition, CO_2-loaded in situ FT-IR tests were performed to evidence thermoresponsive synergetic effects. As clearly seen in Figure 3b, the $–NH_2$ and C–N stretching modes located at the absorption bands of 1579.1 and 1125 cm^{-1} exhibit a slight negative shift but undisturbed diffraction intensity as T_A increases from 348 to 358 K. Such blue frequency shifts but quasi-constant peak intensity indicate that **1a-apz** is actually opposite to conventional porous compounds expected from thermodynamic law, enabling **1a-apz** to be a potential candidate for industrial CO_2 capture under higher T_A.

To better unravel the relationship between flexibility and adsorption behavior at 348 K, in situ CO_2 adsorption coupled with PXRD was recorded (Figure 3c–d). As shown in Figure 3d, the peaks of **1a-apz** indexed as (110) and (300) successively shift to higher degrees upon continued CO_2 pressures, suggesting that a potential self-adaption phenomenon may occur to maximize the capacity of CO_2. The self-adaptive behavior can also be reflected by visualized pore evolution. As shown in Figure S20, the pore conformation of **1a-apz** retrieved from CO_2⊂**1a-apz** at 348 K undergoes obvious structural evolutions accompanied by the aperture expansion with increased CO_2 loading, revealing the dynamic self-adaption of apz. Further, visualized 2D-EDM of CO_2⊂**1a-apz** under various pressures were investigated. As shown in Figure 3e, pressure-dependent 2D-EDM of **1a** remains coincident diffraction spots with the increase of CO_2 loading, indicating inherent rigidity. However, the apz motif inside **1a-apz** channel exhibits a subtle geometry transformation, thereby rendering the expanded diffusion access (colored as light orange), as demonstrated by the diffraction map at 50 and 100 mbar of CO_2 (sections **III** and **IV** in Figure 3e). Note that the planar slice of CO_2⊂**1a-apz** only shows the local 2D-EDM of apz when exposed to 100 mbar of CO_2 (section **IV** in Figure 3e), further indicating the self-adaptive behavior. Also, the CO_2 configurations having both adsorption sites can be decoded by 2D-EDM. Obviously, the diffractive electron density of CO_2 increases with the increasing pressure, as clearly evidenced by the 100 mbar of CO_2 (section **IV** in Figure 3e). To experimentally observe its diffusion process, 2D-EDM yielded from transient PXRD of CO_2⊂**1a-apz** were analyzed under a CO_2 pressure of 0.1 bar. As observed in Figure S21, a concentrated electron density first appears in the central region of the MOF channel at 1 min (Figure S21a), suggesting that the CO_2 diffusion process has occurred. The electron density starts to present non-interfering diffusion footprints and gradually covers the pore channel at 5 min, which can be shown in the cross-sections of the lattice plane along the crystallographic *c*-axis (Figure S21b). Finally, the electron density distribution near the linkers continues to increase at 10 and 20 min, while that in the pore center tends to decrease (Figure S21c–d), indicating that CO_2 prefers to diffuse into the pore surface rather than staying in the pore center.

We further combined Grand Canonical Monte Carlo (GCMC) approach to explore the binding interaction. As observed in Figure S22a–b, the density spots of CO_2 confirm that it prefers to adsorb at the confined space near the linkers. Such adsorption locations are in accordance with the results yielded from experimental 2D-EDM, which is conducive to constructing unimpeded diffusion channels for boosting CO_2 diffusion. The geometries were also optimized using DFT to determine possible adsorption mechanisms. As demonstrated in Figure 3f, two CO_2 molecules (**Site A** and **B**) having distinct binding orientations are accommodated in the pillar-shaped channels, and they adopt a quasi-orthogonal stacking (Figure S23). The CO_2 confined in **Site A** is spatially aligned at a tilted angle along the crystallographic *c*-axis and well confined through multiple binding interactions (section **I** in Figure 3f). In detail, the terminal oxygen atoms in CO_2 are well captured through a strong π-complexation effect with open Mg^{2+} sites and interact side-on to the ligand through van der Waals interactions (C=O···π), giving the binding distances of 3.02 Å (D1) and 2.84 Å (D2). Meanwhile, the coterminous carbon atom in the C=O fragment is tightly grasped by forming strong Lewis acid/base interactions with circumambient electronegative amino motifs, affording the bonding distances of 3.24 (D3) and 3.78 Å (D4). On the other hand, the CO_2 located at **Site B** shows an orthogonal adsorption orientation to the *c*-axis and is also grasped through multiple binding affinities (section **II** in Figure 3f). Similarly, a strong π-complexation effect with an $Mg^{\delta+}$–$O^{\delta-}$ binding distance of 2.45 Å (D1) is formed, yielding the tilted angle of 86.1° between linear CO_2 and *c*-axis direction (Figure S24). The carbon atom is tightly confined by forming the Lewis acid/base interactions with bilateral amino motifs, giving the shorter distances of 2.53 Å (D2) and 3.89 Å (D3). Also, there are indispensable van der Waals interactions between the terminal oxygen atom and the benzene ring, with binding distances of 3.24 Å (D4) and 3.56 Å (D5), respectively. Comparing the adsorption conformation at 298 K (Figure S25), it can be observed that two CO_2 molecules display approximate-orthogonal packing models, giving a dihedral angle of 96.8° (section **I** in Figure S25). For the CO_2 in **Site A**, it prefers to accommodate in the pore center through a combination of multiple Lewis acid/base interactions (distance: 3.62 Å for D1, 3.74 Å for D2, and 3.66 Å for D3), van der Waals interaction (C=O···π, 3.28 Å for D4), and underlying intermolecular interaction (2.87 Å for D5) (section **II** in Figure S25). Noteworthy, the other isolated CO_2 immobilized in **Site B** still adopts quasi-perpendicular binding orientation to the *c*-axis with the included angle of 88.4° (section **III** in Figure S25). The spatial array perpendicular to the *c*-axis dimension will maximize its binding interactions with surrounding screening sites comprising π-complexation effect and Lewis acid/base interactions (section **IV** in Figure S25).

The binding affinity could be further evidenced by evaluating the binding energies (E_B). Not surprisingly, the total E_B at 298 K (48.4 kJ mol^{-1}) is slightly higher than that at 348 K (40.6 kJ mol^{-1}), owing to the exothermic physical adsorption process. However, an in-depth insight into the adsorption heat at each site reveals that the E_B at **Site B** follows an unusual hierarchy of 28.3 kJ mol^{-1} at 348 K >

18.4 kJ mol^{-1} at 298 K. On the basis of the above analyses, we deduced that the atypical E_B mainly originated from **1a-apz** adapting aptly with increased temperature to yield local self-adaptive microenvironment for forming CO_2-specific induced fits (aka "induced-fit-identification"), a unique adsorption behavior similar to "enzyme-substrate" (Figure S26).[25] The ESP distributions around **Site B** were herein mapped by applying DFT calculations to understand the unusual "induced-fit-identification", where the contour maps of blue and red correspond to positive and negative potentials, respectively (Figure 3f). Apparently, the positive/negative regions with lower potentials are dispersedly distributed around **Site B** at 298 K (section **III** in Figure 3f). However, at 348 K, the reconfigured ESP is relatively concentrated around **Site B** (section **IV** in Figure 3f), showing enhanced positive potentials near open Mg^{2+} sites and negative potentials near dobdc^{4-}. Undoubtedly, such an ESP reconfiguration will favorably affect the binding orientation of adsorbed CO_2 and enhance its binding affinity with the pore surface through the complementary ESP effect (Figure S27). To our knowledge, this is the first time that a complementary ESP effect other than self-adaptive and multiple sites is applied to jointly initiate the unusual "induced-fit-identification", being different from the similar induced-fit effects reported so far (Table S6).

To further verify the proposed "induced-fit-identification" mechanism simulated by the DFT method, in situ HR-SXRD of CO_2-loaded **1a-apz** and Rietveld refinements were conducted (Figure S28 and Table S7). As demonstrated in Figure S29, the resolved binding configurations of CO_2⊂**1a-apz** at 298 K are basically consistent with the DFT-calculated results (Figure S25). However, for CO_2⊂**1a-apz** at 348 K (Figure S30), an emerging adsorption site (denoted as **Site C**) was observed based on HR-SXRD data in comparison with the theoretical result (Figure 3f). This experimentally identified adsorption site is due to π-complexation effect with open Mg^{2+} sites (2.62 Å for D1) and Lewis acid/base interactions (3.05 for D2; 2.88 Å for D3).

Motivated by the unique "induced-fit-identification" in **1a-apz**, we analyzed its separation performance for CO_2/CO (1/99, v/v). Ideal adsorbed solution theory (IAST) selectivity was first predicted by fitting the double-site Langmuir–Freundlich (DSLF) models (Table S8).[26] As shown in Figure 4a, **1a-apz** suggests a noticeable IAST selectivity for CO_2/CO mixtures, yielding an ultrahigh value of 2023 at near-zero coverage and 298 K, which is far superior to well-known MOFs, including ZJU-HOF-1 (15),[9a] DMOF-1 (55),[4] and HKUST-1 (5),[4] albeit being slightly lower than SIFSIX-3-Ni (4044),[4] which has a quasi-sieving effect. Note that the approach is usually subject to limited requirements or uncertainties; thus, errors may occur due to narrow pores (nonideal gas solution) and structural flexibility.[27] Consequently, IAST selectivity was evaluated here just for qualitative analysis. Further, breakthrough tests were conducted to assess the CO_2/CO separation performance. First, transient breakthrough simulations at 298 K and 1 bar were predicted to assess the feasibility. Simulated results reveal the distinct breakthrough profiles for **1a-pz** and **1a-apz** (Figure 4b). Especially for **1a-apz**, CO is first to elute through the bed while CO_2 experiences prolonged break-

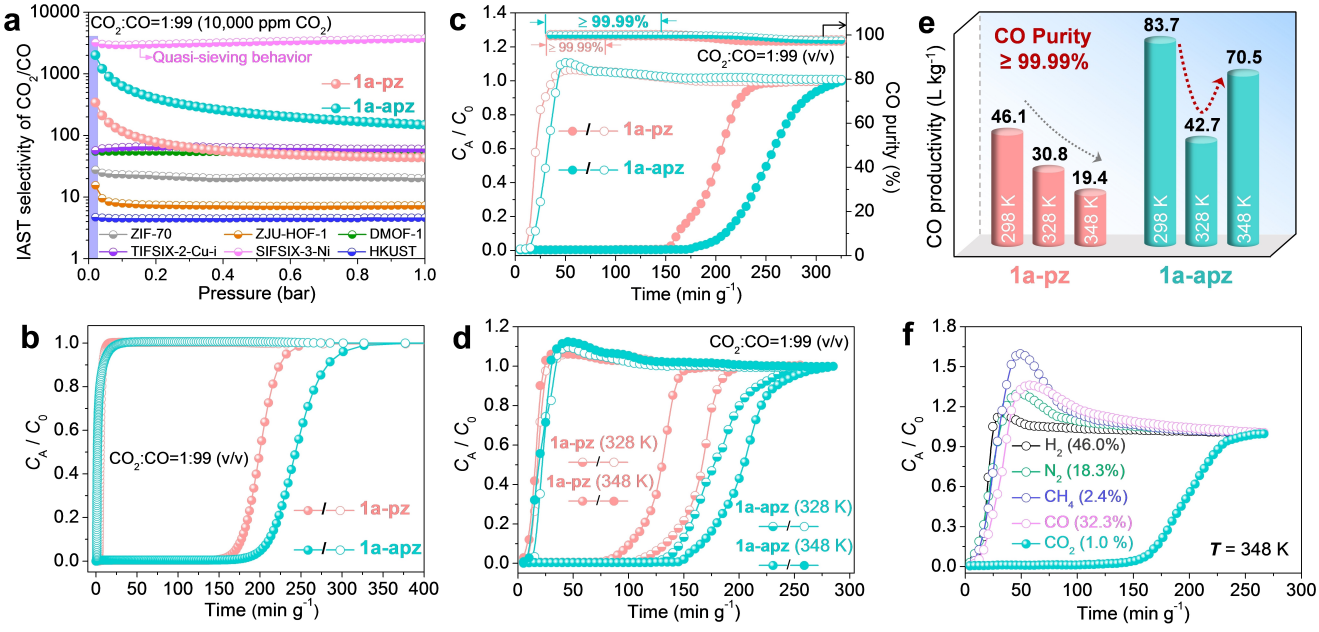

Figure 4. (a) IAST selectivities of CO_2/CO (1/99, v/v) at 298 K on **1a-apz** and some selected materials; (b) Simulated breakthrough curves of **1a-pz** and **1a-apz** for CO_2/CO (1/99, v/v) at 298 K; (c) Experimental breakthrough curves of **1a-pz** and **1a-apz** for CO_2/CO (1/99, v/v) at 298 K and 1 bar; (d) Experimental breakthrough curves of **1a-pz** and **1a-apz** for CO_2/CO (1/99, v/v) at 328 and 348 K and 1 bar; (e) CO productivity of **1a-pz** and **1a-apz** at variable temperatures, with the CO purity exceeding 99.99%; (f) Experimental breakthrough curves of **1a-apz** for quinary $H_2/N_2/CH_4$/CO/CO_2 (46/18.3/2.4/32.3/1, v/v/v/v/v) mixtures at 348 K and 1 bar.

through time, thus achieving efficient CO_2/CO separation performance.

We further performed experimental breakthrough tests with CO_2/CO (1/99, v/v) mixtures flowing over the lab-customized column. Likewise, CO fraction first broke out from both **1a-pz** and **1a-apz** in a short breakthrough time of ca. 7.8 and 13.1 min g^{-1}, while CO_2 was still retained for a long time, giving the breakthrough time of 150 min g^{-1} for **1a-pz** and 175 min g^{-1} for **1a-apz** (Figure 4c). Note that the simulated curves (Figure 4b) are somewhat sharper than those observed experimentally, mainly because intracrystalline diffusional influences were ignored in the simulations.[13,27] Notably, ultrapure CO purity ($\geq$99.99 %) can be achieved at 298 K (Figure 4c), far exceeding that required for STO ($\geq$99.5 %), indicative of great potential in ultra-pure CO enrichment.

We performed breakthrough tests at 328 and 348 K to verify the separation potential at higher T_A. As observed in Figure 4d, the breakthrough time of CO_2 for **1a-pz** reduces as temperature increases from 328 to 348 K, yet increases for **1a-apz** under identical conditions, suggesting that the CO_2 capture ability of **1a-apz** at 348 K is superior to that at 328 K. The attractive results prompted us to calculate CO productivity with a purity of $\geq$99.99 %, a crucial but easily overlooked indicator to evaluate CO quality. Apparently, the CO productivity of **1a-apz** is up to 83.7 L kg^{-1} at 298 K (Figure 4e). Notably, the productivity decreases to 42.7 L kg^{-1} at 328 K but reversely increases to 70.5 L kg^{-1} at 348 K in contrast to the trend of adsorption isotherms of CO (Figure S16a). Considering the above results, we believe that the kinetic diffusion at 348 K may award **1a-apz** with important effects for promoting CO_2 capture. Herein, time-dependent kinetic adsorption profiles of CO_2 and CO on **1a-apz** were collected at 100 mbar and 328–348 K (Figure S31a–d). Expectedly, **1a-apz** took the shortest time to attain saturated CO_2 capacity at 348 K (Figure S31b), giving the faster diffusivity coefficient (1.11×10^{-14} m^2 s^{-1}), which is 4.4 times higher than that at 328 K (2.5×10^{-15} m^2 s^{-1}). More importantly, the derived diffusion selectivity of CO_2/CO is up to 10.7 at 348 K, almost 4.1 times higher than that at 328 K (2.64). Therefore, the faster diffusion behavior endows **1a-apz** with a collaborative impetus for reinforcing trace CO_2 capture and purifying CO. Such a kinetic-driven effect is vital, given that industrial separation units actually operate under nonequilibrium conditions.[27–28] Notably, the breakthrough tests of quinary syngas consisting of H_2 (46 %), N_2 (18.3 %), CH_4 (2.4 %), CO (32.3 %), and CO_2 (1 %)[7] also reveal that ppm-level CO_2 can still be exclusively trapped by **1a-apz** at 348 K, whereas H_2, N_2, CH_4, and CO elute first (Figure 4f). The results render **1a-apz** capable of removing ppm level CO_2 impurity from the complicated syngas stream, demonstrating its great potential in upgrading syngas.

Conclusion

In this work, we target a thermoresponsive MOF (**1a-apz**) that realizes ppm-level CO_2 removal and ultra-pure CO enrichment through an unusual induced-fit-identification under practical T_A. Adsorption results suggest an ultra-high CO_2 capacity of 145.0/197.6 cm^3 g^{-1} (0.01/0.1 bar) for **1a-apz** at 298 K. Interestingly, the capacity of CO_2 does not decrease significantly when T_A increases from 328 to 348 K. Comprehensive variable-temperature tests, including VT-PXRD, VT-Raman, VT-FTIR, and ^{15}N solid-state NMR, explicitly unravel the atypical behavior of **1a-apz** that originates from the local rotation of apz motif in response to higher T_A. CO_2-loaded in situ Raman and FT-IR results indicate that dynamic flexibility of apz exerts an important effect on CO_2 capture at 348 K. In situ high-resolution synchrotron, two-dimensional electron-density map, and modeling simulations jointly confirm that an unusual induced-fit-identification is responsible for ppm-level CO_2 removal, attributing to the synergistic effects comprising self-adaptive behavior of apz motif, multiple binding sites, and electrostatic potential reconfiguration. Breakthrough tests reveal that **1a-apz** can remove trace CO_2 from 1/99 CO_2/CO mixtures, affording a high CO productivity of 70.5 L kg^{-1} for **1a-apz** with ultrahigh purity of $\geq$99.99 % at 348 K and 1 bar. The excellent property was also validated by quinary crude syngas containing $H_2/N_2/CH_4/CO/CO_2$ (46/18.3/2.4/32.3/1, v/v/v/v/v), suggesting its great potential for trace CO_2 removal and ultra-pure CO enrichment from syngas.

Acknowledgements

This work was financially supported by the National Key Research and Development Program Nanotechnology Specific Project (No. 2020YFA0210900), National Natural Science Foundation of China (No. 21938001, 21961160741), Guangdong Provincial Key R&D Program (2019B110206002), Local Innovative and Research Teams Project of Guangdong Pearl River Talents Program (2017BT01 C102), the Ministry of Education-Singapore (MOE2019-T2-1-093, MOE-T2EP10122-0002), the Energy Market Authority of Singapore (EMA-EP009-SEGC-020), the Agency for Science, Technology and Research (U2102d2004, U2102d2012), and National Research Foundation Singapore (NRF-CRP26-2021RS-0002). Peng Hu is also grateful to the China Scholarship Council (CSC) for the financial support (202106380115). We also thank Prof. Xiaolong Li and his team for the kind advice on this project at the beamlines BL02U2 of Shanghai Synchrotron Radiation Facility (SSRF) for assisting with the SXRD data collection and analysis.

Conflict of Interest

The authors declare no conflict of interest.

Data Availability Statement

The data that support the findings of this study are available from the corresponding author upon reasonable request.

Keywords: CO_2/CO Separation · Induced-Fit-Identification · Metal-Organic Frameworks · Syngas Purification · Thermoresponsive Effect

[1] Y. Huang, H. Ma, Z. Xu, W. Qian, H. Zhang, W. Ying, *RSC Adv.* **2021**, *11*, 13876–13884.

[2] M. S. Fan, A. Z. Abdullah, S. J. C. Bhatia, *ChemCatChem* **2009**, *1*, 192–208.

[3] A. Evans, R. Luebke, C. Petit, *J. Mater. Chem. A* **2018**, *6*, 10570–10594.

[4] K. J. Chen, Q. Y. Yang, S. Sen, D. G. Madden, A. Kumar, T. Pham, K. A. Forrest, N. Hosono, B. Space, S. Kitagawa, M. J. Zaworotko, *Angew. Chem. Int. Ed.* **2018**, *57*, 3332–3336.

[5] P. Hu, H. Wang, C. Xiong, H. Liu, J. Han, J. Zhou, Z. Zhao, Y. Wang, H. Ji, *ACS Sustainable Chem. Eng.* **2021**, *9*, 15897–15907.

[6] a) A. Luna-Triguero, J. M. Vicent-Luna, M. J. Jansman, G. Zafeiropoulos, M. N. Tsampas, M. C. M. van de Sanden, H. N. Akse, S. Calero, *Catal. Today* **2021**, *362*, 113–121; b) G. D. Wang, R. Krishna, Y. Z. Li, W. J. Shi, L. Hou, Y. Y. Wang, Z. Zhu, *Angew. Chem. Int. Ed.* **2022**, *61*, e202213015.

[7] Y. Zhou, Y. Shen, Q. Fu, D. Zhang, *Ind. Eng. Chem. Res.* **2017**, *56*, 6741–6754.

[8] a) P. Hu, R. Wang, Z. Gao, S. Jiang, Z. Zhao, H. Ji, Z. Zhao, *Appl. Catal. B* **2021**, *296*, 120371; b) P. Hu, Z. Zhao, X. Sun, Y. Muhammad, J. Li, S. Chen, C. Pang, T. Liao, Z. Zhao, *Chem. Eng. J.* **2019**, *356*, 329–340; c) T. He, X.-J. Kong, Z.-X. Bian, Y.-Z. Zhang, G.-R. Si, L.-H. Xie, X.-Q. Wu, H. Huang, Z. Chang, X.-H. Bu, M. Zaworotko, Z.-R. Nie, J.-R. Li, *Nat. Mater.* **2022**, *21*, 689–695; d) R. L. Siegelman, E. J. Kim, J. R. J. Long, *Nat. Mater.* **2021**, *20*, 1060–1072.

[9] a) J. X. Wang, J. Pei, X. W. Gu, Y. X. Lin, B. Li, G. Qian, *Chem. Commun.* **2021**, *57*, 10051–10054; b) H. Cao, S. Wang, Y. Wang, H. Lyu, R. Krishna, Z. Lu, J. Duan, W. Jin, *CrystEngComm* **2017**, *19*, 6927–6931; c) A. Evans, M. Cummings, D. Decarolis, D. Gianolio, S. Shahid, G. Law, M. Attfield, D. Law, C. Petit, *RSC Adv.* **2020**, *10*, 5152–5162.

[10] Y. Chen, Y. Yang, Y. Wang, Q. Xiong, J. Yang, S. Xiang, L. Li, J. Li, Z. Zhang, B. Chen, *J. Am. Chem. Soc.* **2022**, *144*, 17033–17040.

[11] M. H. Yu, B. Space, D. Franz, W. Zhou, C. He, L. Li, R. Krishna, Z. Chang, W. Li, T. L. Hu, X. H. Bu, *J. Am. Chem. Soc.* **2019**, *141*, 17703–17712.

[12] Y. He, J. Shang, Q. Gu, G. Li, J. Li, R. Singh, P. Xiao, P. A. Webley, *Chem. Commun.* **2015**, *51*, 14716–14719.

[13] P. Hu, H. Liu, H. Wang, J. Zhou, Y. Wang, H. Ji, *J. Mater. Chem. A* **2022**, *10*, 881–890.

[14] S. E. Henkelis, S. M. Vornholt, D. B. Cordes, A. M. Slawin, P. S. Wheatley, R. Morris, *CrystEngComm* **2019**, *21*, 1857–1861.

[15] Z. Zhang, Q. Ding, J. Cui, X. Cui, H. Xing, *Sci. China Mater.* **2021**, *64*, 691–697.

[16] S. Mukherjee, N. Sikdar, D. O'Nolan, D. M. Franz, V. Gascon, A. Kumar, N. Kumar, H. S. Scott, D. G. Madden, P. E. Kruger, B. Space, M. J. Zaworotko, *Sci. Adv.* **2019**, *5*, eaax9171.

[17] a) H. Zeng, M. Xie, Y. L. Huang, Y. Zhao, X. J. Xie, J. P. Bai, M. Y. Wan, R. Krishna, W. Lu, D. Li, *Angew. Chem. Int. Ed.* **2019**, *58*, 8515–8519; b) T. M. McDonald, J. A. Mason, X. Kong, E. D. Bloch, D. Gygi, A. Dani, V. Crocella, F. Giordanino, S. O. Odoh, W. S. Drisdell, B. Vlaisavljevich, A. L. Dzubak, R. Poloni, S. K. Schnell, N. Planas, K. Lee, T. Pascal, L. F. Wan, D. Prendergast, J. B. Neaton, B. Smit, J. B. Kortright, L. Gagliardi, S. Bordiga, J. A. Reimer, J. R. Long, *Nature* **2015**, *519*, 303–308; c) K. S. Walton, A. R. Millward, D. Dubbeldam, H. Frost, J. J. Low, O. M. Yaghi, R. Q. Snurr, *J. Am. Chem. Soc.* **2008**, *130*, 406–407; d) M. L. Foo, R. Matsuda, Y. Hijikata, R. Krishna, H. Sato, S. Horike, A. Hori, J. Duan, Y. Sato, Y. Kubota, M. Takata, S. Kitagawa, *J. Am. Chem. Soc.* **2016**, *138*, 3022–3030.

[18] R. Vismara, G. Tuci, A. Tombesi, K. V. Domasevitch, C. Di Nicola, G. Giambastiani, M. R. Chierotti, S. Bordignon, R. Gobetto, C. Pettinari, A. Rossin, S. Galli, *ACS Appl. Mater. Interfaces* **2019**, *11*, 26956–26969.

[19] I. G. Shenderovich, G. Buntkowsky, A. Schreiber, E. Gedat, S. Sharif, J. Albrecht, N. S. Golubev, G. H. Findenegg, H.-H. Limbach, *J. Phys. Chem. B* **2003**, *107*, 11924–11939.

[20] a) Q. Gao, J. Xu, D. Cao, Z. Chang, X. H. Bu, *Angew. Chem. Int. Ed.* **2016**, *55*, 15027–15030; b) V. N. Vukotic, K. J. Harris, K. Zhu, R. W. Schurko, S. J. Loeb, *Nat. Chem.* **2012**, *4*, 456–460.

[21] Q. Tan, H. Huang, Y. Peng, Y. Chang, Z. Zhang, D. Liu, C. Zhong, *J. Mater. Chem. A* **2019**, *7*, 26574–26579.

[22] M. Frisch, G. Trucks, H. Schlegel, G. Scuseria, M. Robb, J. Cheeseman, G. Scalmani, V. Barone, B. Mennucci, G. Petersson, Gaussian Inc. Wallingford CT, **2010**.

[23] I. Strauss, A. Mundstock, D. Hinrichs, R. Himstedt, A. Knebel, C. Reinhardt, D. Dorfs, J. Caro, *Angew. Chem. Int. Ed.* **2018**, *57*, 7434–7439.

[24] F. Zheng, D. N. Tran, B. J. Busche, G. E. Fryxell, R. S. Addleman, T. S. Zemanian, C. L. Aardahl, *Ind. Eng. Chem. Res.* **2005**, *44*, 3099–3105.

[25] D. E. Koshland Jr, *Proc. Natl. Acad. Sci. USA* **1958**, *44*, 98–104.

[26] a) P. Hu, J. Hu, H. Wang, H. Liu, J. Zhou, Y. Liu, Y. Wang, H. Ji, *ACS Appl. Mater. Interfaces* **2022**, *14*, 15195–15204; b) P. Hu, J. Han, J. Zhou, H. Wang, C. Xiong, H. Liu, X. Zhou, Y. Wang, H. Ji, *Chem. Eng. J.* **2021**, *426*, 131302; c) D. E. Jaramillo, D. A. Reed, H. Z. Jiang, J. Oktawiec, M. W. Mara, A. C. Forse, D. J. Lussier, R. A. Murphy, M. Cunningham, V. Colombo, D. K. Shuh, J. A. Reimer, J. R. Long, *Nat. Mater.* **2020**, *19*, 517–521; d) G. L. Smith, J. E. Eyley, X. Han, X. Zhang, J. Li, N. M. Jacques, H. G. Godfrey, S. P. Argent, L. J. McCormick McPherson, S. J. Teat, Y. Cheng, M. D. Frogley, G. Cinque, S. J. Day, C. C. Tang, T. L. Easun, S. Rudić, A. J. Ramirez-Cuesta, S. Yang, M. Schröder, *Nat. Mater.* **2019**, *18*, 1358–1365.

[27] P. Hu, J. Hu, H. Liu, H. Wang, J. Zhou, R. Krishna, H. Ji, *ACS Cent. Sci.* **2022**, *8*, 1159–1168.

[28] a) C. C. K. Beh, P. A. Webley, *Adsorpt. Sci. Technol.* **2003**, *21*, 35–52; b) C. C. Beh, P. Webley, *Ind. Eng. Chem. Res.* **2003**, *42*, 5287–5292.

[29] Deposition numbers 2264297 (As-synthesized **1a-pz**), 2264296 (As-synthesized **1a-apz**), 2264298 (CO_2-loaded **1a-apz** at 298 K) and 2264299 (CO_2-loaded **1a-apz** at 348 K) contain the supplementary crystallographic data for this paper. These data are provided free of charge by the joint Cambridge Crystallographic Data Centre and Fachinformationszentrum Karlsruhe Access Structures service.

Manuscript received: April 27, 2023
Accepted manuscript online: June 13, 2023
Version of record online: July 3, 2023

Angewandte Chemie
Eine Zeitschrift der Gesellschaft Deutscher Chemiker

Supporting Information

Induced-Fit-Identification in a Rigid Metal-Organic Framework for ppm-Level CO_2 Removal and Ultra-Pure CO Enrichment

P. Hu, J. Hu, M. Zhu, C. Xiong, R. Krishna, D. Zhao, H. Ji**

Table of Contents

Chemicals and reagents

The chemicals and solvents in this work were directly purchased without further purification. Magnesium nitrate hexahydrate ($Mg(NO_3)_2 \cdot 6H_2O$, AR, 95%), 2,5-dihydroxybenzene-1,4-dicarboxylic acid (H_4dobdc, AR, 98%), pyrazine ($C_4H_4N_2$, AR, 98%), 2-aminopyrazine ($C_4H_5N_3$, AR, 97%), sodium hydroxide (NaOH, AR, 97%), and sodium acetate (CH_3COONa, AR, 98%) were obtained from Aladdin Reagent. Ethanol (CH_3CH_2OH, 99.5%), N,N-dimethylformamide (C_3H_7NO, DMF, 99.8%), and deionized water were purchased from LiGe Reagent.

Preparation of pristine Mg-MOF nanocrystal (1a)

1a nanocrystal was prepared based on our previous report with minor modifications.[1] In brief, $Mg(NO_3)_2 \cdot 6H_2O$ (0.49 g, 1.91 mmol), H_4dobdc (0.018 g, 0.09 mmol), and sodium acetate (0.42 g, 4.94 mmol) were first dissolved in the mixed solution containing DMF (8 mL), ethanol (8 mL), and water (7.6 mL). Subsequently, the mixture was placed into a microwave reactor with reflux condensation and heated at 398 K for 60 min. The obtained product was washed with DMF and methanol six times to remove unreacted ligands and remaining impurities. At last, the prepared sample (labeled as **1a**) was dried in an air dry oven at 358 K for 12 h and then heated at 373 K for 24 h in a vacuum oven to afford a light brown powder (0.63 g, yield 67.9%).

Preparation of pz-functionalized Mg-MOF nanocrystal (1a-pz)

The activated **1a** sample (0.33 g) and pz (0.063 g, 0.79 mmol) (pz = pyrazine) powders were put into a lab-customized glass tube, then the powders together with the glass tube were heated in a vacuum oven at a constant temperature of 363 K for 8 h. During heating, solid pz powders could be evaporated into gaseous pz vapor, which could further form coordinated bonds with the unoccupied Mg^{2+} sites of **1a** to afford pz-engineered **1a-pz**. After that, the reaction temperature was cooled down to room temperature, and the powder was immersed in 50 mL of methanol for 3 h and kept stirring at 300 rpm to dissolve unreacted pz impurities. Then, the solution was centrifuged and repeatedly washed with methanol four times to remove the remaining pz impurities. At last, the obtained **1a-pz** was dried in an air-dry oven at 358 K for 12 h and then heated at 363 K for 24 h in a vacuum oven to afford a light brown powder (0.356 g, yield 90.6%).

Preparation of apz-functionalized Mg-MOF nanocrystal (1a-apz)

The activated **1a** sample (0.33 g) and apz (0.067 g, 0.71 mmol) (apz = 2-aminopyrazine) powders were put into a lab-customized glass tube, then the powders together with the glass tube were heated in a vacuum oven at a constant temperature of 383 K for 10 h. During heating, solid apz powders could be evaporated into gaseous apz vapor, which could further form coordinated bonds with the unoccupied Mg^{2+} sites of **1a** to afford apz-engineered **1a-apz**. After that, the reaction temperature was cooled down to room temperature, and the powder was immersed in 50 mL of methanol for 5 h and kept stirring at 300 rpm to dissolve unreacted apz impurities. Then, the solution was centrifuged and repeatedly washed with methanol four times to remove the remaining apz impurities. At last, the obtained **1a-apz** was dried in an

air-dry oven at 358 K for 12 h and then heated at 383 K for 24 h in a vacuum oven to afford a light brown powder (0.354 g, yield 89.2%).

Gas sorption tests

N_2 sorption isotherms of the samples were tested at 77 K (ASAP2460, Micromeritics). Each sample (150 mg) was initially degassed at 120 °C for 24 h under vacuum before the test. Single-gas adsorption experiments of various guests were conducted on the Micromeritics ASAP2020 instrument. All gases used in this work exceeded 99.99% purity. Kinetic adsorption profiles of CO_2 and CO were tested using the Intelligent Gravimetric Analyzer (IGA-100, HIDEN). Activated **1a-pz** or **1a-apz** (100 mg each) were first vacuum-activated at 120 °C for 6 h. When the analysis started, pure CO_2 or CO was introduced and tested at a given pressure of 100 mbar.

Column breakthrough experiments

The column breakthrough experiments were tested in a stainless steel column (10.0 mm I.D. × 200 mm length) manually packed with activated samples (1.022 g) and filled the void space with silica wool. Before the breakthrough tests, the column was *in-situ* heated by helium (He) gas (rate: 5 sccm) at 393 K for 12 h to activate the samples. Then, the column was cooled down, and He (rate: 5 sccm) was continued to purge the samples for 10~12 h. After that, the gas mixture of CO_2/CO (1/99, v/v) or $H_2/N_2/CH_4/CO/CO_2$ (46/18.3/2.4/32.3/1, v/v/v/v/v) was introduced into the column. After the experimental tests, the adsorbent could be further regenerated through *in-situ* heating of the column under a flowing He (rate: 10.0 sccm) for 5 h at 423 K. The outlet gas from the column was monitored online through GC.

***In-situ* variable-temperature Raman spectroscopy**

In-situ variable-temperature Raman spectroscopy tests of bare **1a-apz** were performed using the Thermo Scientific DXR Raman microscope with a laser excitation wavelength of 532 nm and attached XPH-300 hot stage. The Raman spectra were collected from 3500 to 50 cm^{-1} at the heating rate of 5 °C min^{-1}. The samples were placed in a glass sheet using a 50 μm pinhole spectrograph aperture. The Raman spectra were obtained after 2 min of stabilization at each temperature. For *in-situ* variable-temperature Raman spectroscopy tests of CO_2-loaded **1a-apz**, the sample was performed using a Horiba HR Evolution coupled with a laser at 532 nm, and Linkam THMS600 stage was used to control the testing temperature, which can be controlled from 298 to 358 K. The sample was placed into the platinum crucible (diameter: 5.0 mm, depth: 3.0 mm) and then heated in the electric furnace.

***In-situ* variable-temperature powder X-ray diffraction (PXRD) tests**

In-situ variable-temperature PXRD tests were collected using the Bruker D8 Advance X-ray diffractometer. The Anton Paar XRK 900 sample holder coupled with TCU 750 temperature control unit under N_2 flow (30 sccm) was used to control the temperature.

In-situ PXRD/CO_2 adsorption measurements

In-situ PXRD/CO_2-adsorption measurements were collected on the Rigaku SmartLab X-ray diffractometer with Cu-Ka radiation connected to MicrotracBEL Max instrument, and each PXRD pattern was collected at a step of 0.02° and a scan speed of 8° min^{-1} after each isotherm data point was collected.

High-resolution synchrotron X-ray diffraction (HR-SXRD)

HR-SXRD experiments were performed on the beamline BL02U2 (X-ray wavelength of 0.6887 Å) at Shanghai Synchrotron Radiation Facility (SSRF). The beam size was confined by horizontal and vertical slits to be approximately 0.3 × 0.3 mm^2. The two-dimensional HR-SXRD signal was obtained by a PILATUS3S 2M detector. In addition, a special coin cell was designed for *in-situ* HRXRD study. There were two observation holes with a radius of ~2 mm in the middle of both sides of the cell, guaranteeing that X-rays could penetrate through the active material during operation. The special *in-situ* cell observation hole was sealed with polyimide tape. For *in-situ* CO_2 adsorption experiments, the flow rate of CO_2 into the sample tank was controlled at 4 sccm, and the testing pressure of CO_2 was kept at 400 ± 5 mbar. Besides, the ambient temperature in the sample tank was realized by programmed heating. The peak positions and pattern indexation were extracted to complete the structural model, and final Rietveld refinements were carried out with isotropic displacement parameters for all atoms. The final crystallographic files of **1a-pz**, **1a-apz**, and CO_2 loaded **1a-apz** were obtained from Rietveld refinements of HR-SXRD data and further structural optimization using DFT method. Note that the structural symmetry was eliminated to ensure the convergence of the system.

In-situ variable-temperature FT-IR spectroscopy

In-situ variable-temperature FT-IR spectra of **1a-apz** were collected using an IS10 FT-IR instrument (Nicolet, QC, Canada). Before the measurements, the self-supporting sorbent wafer (ca. 10 mg) was evacuated at room temperature for 1 h. The sample was exposed to CO_2 for 20 h under the given pressure of 1.0 bar to ensure that the adsorption process had reached equilibrium. FT-IR spectra were then collected in the range of 4000~400 cm^{-1} with increasing the testing temperature.

Computational simulation

For the as-prepared **1a**, the crystallographic data in CIF format can be indexed from the Cambridge Crystallographic Data Centre (CCDC) under the deposition number 1863524, which can be obtained free of charge via the link https://www.ccdc.cam.ac.uk/structures/. The initial structures of **1a-pz** and **1a-apz** with different models were structured using *Materials Studio* (Accelrys Inc.) program by placing pz or apz in possible locations. Note that the theoretical contents of pz and apz used for modeling were based on experimental ^1H NMR and ICP/EA analysis results to ensure their accuracy. To obtain the optimized geometry locations with lowest energy, all the models were first optimized by molecular mechanics (MM) coupled with the universal force field (UFF). The parameters of unit cells and locations of global metal atoms were fixed in the optimization process. To avoid the possible contacts of pz and apz, the initial models were subjected to 50,000 or 100,000 iterations of energy minimization by smart minimizer. After

the geometry optimization, the systems would reach a more equilibrated state with the lowest energy.[2] During structural optimization, the framework and pz derivatives were considered rigid and flexible, respectively. Besides, the dynamics simulations with fine quality were carried out under the NVT ensemble, and the simulations were performed for 3000 ps at 298 and 348 K. The time step was set at 1 fs, with 300~450 ps run being used to equilibrate the optimized MOF structures and further obtain the thermodynamic energy. Thus, the optimized structures of **1a-pz** and **1a-apz** with the lowest steady-state energy can be regarded as the initial models for further analysis.

To get more precise insights for the hydrogen bonds between pairs of adjacent N-containing motifs, the optimized models obtained from MM simulation were further optimized using the generalized gradient approximation (GGA) with the Perdew-Burke-Ernzerhof (PBE) functional[3] in Dmol^3 module. All electron numerical basis set of double numerical plus polarization (DNP basis set) was used to expand the electronic wave function. DFT semi-core pseudopotentials were applied for core treatment.[4] The energy, force, and displacement convergence criteria were set as 2×10^{-5} Ha, 4×10^{-3} Ha, and 5×10^{-4} Å, and the threshold for SCF density convergence was 1.0×10^{-6}, respectively.

To obtain the gas binding energy, an isolated gas molecule was placed in a cell unit (with the same cell dimensions as the MOF crystal). The static binding energy (at T = 0 K) could be expressed as $E_B = E$ (MOF) + E (gas) - E (MOF + gas).

Crystal structure analysis

PXRD experiments were conducted on the Bruker D8 Advance X-ray diffractometer with Cu Ka emission at room temperature. The Reflex refinements were conducted through the Reflex Module in the *Materials Studio 2019* program. The Rietveld refinements were performed in the 2θ range of 5~40 degree. The initial structural models were produced by referring to the reported single-crystal structure of **1a**. In each refinement, the structures were divided into 3 (metal ion, amino group, and organic ligand), given the fact that a larger number of open Mg^{2+} atoms in the channel and the complete coordination of rigid linkers (dobdc^{4-}) in one unit cell, which can be both treated as rigid motifs during the refinements process, while amino fragments were allowed for motion. These structural freedoms, including the occupancy together with the pseudo-Voigt profile parameters, background parameters, the cell parameters, the zero point of the diffraction pattern, thermal factors, the global isotropic atom displacement parameters, the Berar–Baldinozzi asymmetry correction parameters, etc., were optimized step by step to improve the agreement between the calculated and the experimental powder diffraction patterns.

Grand Canonical Monte Carlo (GCMC) simulation

The preferential binding conformation between guests and MOF structure was initially searched through GCMC simulations. Note that the host framework and the gas molecule were both rigid in GCMC simulations when using the Metropolis method so that the produced host-guest binding energies are equal to adsorption enthalpies. For all the GCMC simulations, the frameworks and the gas molecules were described by the universal forcefield (UFF). Both the equilibration and production steps were set to

5×10^6. The cutoff radius was chosen as 13.0 Å for the Lennard-Jones (LJ) potential, and the long-range electrostatic interactions were handled by the Ewald & Group summation method. The Mulliken charges and ESP charges, calculated by PDFT, were employed for the framework atoms and guest atoms, respectively.

Transient breakthrough simulations

The performance of industrial fixed bed adsorbers is dictated by a combination of adsorption selectivity and uptake capacity. Transient breakthrough simulations were carried out for CO_2/CO (1/99, v/v) mixtures operating at a total pressure of 100 kPa and T = 298 K, using the methodology described in earlier publications.[5]

Calculation of rotational barrier

The energy barriers for the rotation and flipping of pz and apz rings in the MOF skeleton were calculated using Gaussian 09 program.[6] Geometry optimization and vibrational frequency calculations were carried out using the DFT method with the dispersion-corrected[7] B3LYP functional (B3LYP-D3). The 6-311G(d,p) basis sets were used for all atoms. Further, the rotation barrier was estimated by scanning the potential energy surface (PES), in which the dihedral angle ($Mg^{336}N^{422}C^{421}C^{420}$) in pz and apz molecules was changed with an interval of 5°.

Calculations of ideal adsorbed solution theory

Dual-site Langmuir-Freundlich isotherm model was first adopted to fit the single-component loadings at 298 K, as shown in Equations 1 and 2:

$$q = N_1 \frac{ap^b}{1+ap^b} + N_2 \frac{cp^d}{1+cp^d} \quad (1)$$

With T-dependent parameters a and c,

$$a = a_0 exp\left(\frac{E_A}{RT}\right);\ c = c_0 exp\left(\frac{E_B}{RT}\right) \quad (2)$$

Here, p is the pressure of the bulk gas at equilibrium with the adsorbed phase (kPa), q is the adsorbed amount per mass of adsorbent (mol kg^{-1}), N_1 *and* N_2 are the saturation capacities (mol kg^{-1}) of two different binding sites, a and c (1 kPa^{-1}) are the corresponding adsorption equilibrium constants reflecting the affinity coefficients of sites 1 and 2, and b and d represent the deviations from an ideal homogeneous surface for site 1 and 2.

The gas adsorption selectivity at 298 K and 1 bar was calculated using ideal adsorbed solution theory (IAST) on the basis of the single-component adsorption data. The adsorption selectivity for CO_2/CO separation is defined by Equation 3:

$$S_{ads} = \frac{q_1/q_2}{p_1/p_2} \quad (3)$$

In the above equation, the fitting parameters q_1 and q_2 reflected the molar adsorption in the adsorbed

phase in equilibrium with the bulk gas phase with partial p_1 and p_2. In this work, a dual-site Langmuir-Freundlich (DSLF) model was applied to fit CO_2 and CO isotherms.

Calculations of isosteric heat

The isosteric heat (Q_{st}), being the crucial thermodynamic variable in the adsorption process, affords important information about the binding affinity between the adsorbate molecules and the adsorbent surfaces at different coverage. For this sake, the coverage-dependent adsorption enthalpy was evaluated by adopting a virial fitting method. In detail, a virial-type equation mainly contains parameters a_i and b_i, which are independent of temperature. In the equation, a_i and b_i represent the virial fitting coefficients, m and n stand for the numbers of coefficients needed to precisely describe the isotherms, as shown in Equation 4:[1]

$$\ln P = \ln n + \frac{1}{T}\sum_{i=0}^{l} a_i n^i + \sum_{j=0}^{m} b_j n^j \quad (4)$$

The value of isosteric heat (Q_{st}) could be calculated following the Clausius-Clapeyron equation, as defined in Equation 5:

$$Q_{st} = -R\left[\frac{\partial \ln p}{\partial(1/T)}\right]_n = -R\sum_{i=0}^{l} a_i n^i \quad (5)$$

Calculations of diffusion coefficients

Micropore diffusion formula was adopted to investigate the adsorption kinetics based on the kinetic curve. The intraparticle diffusion equation could be expressed by Equation 6:[8]

$$\frac{Q_t}{Q_e} = \frac{6}{r_c}\sqrt{\frac{D_M t}{\pi}} \quad (6)$$

In this equation, D_M (cm^2/s) reflects the intracystalline diffusion coefficient, and r_c (nm) is the crystal radius. The diffusion time constant (D_M / r_c^2, s^{-1}) was achieved from the slope of Q_t / Q_e versus t.

Supplementary Figures

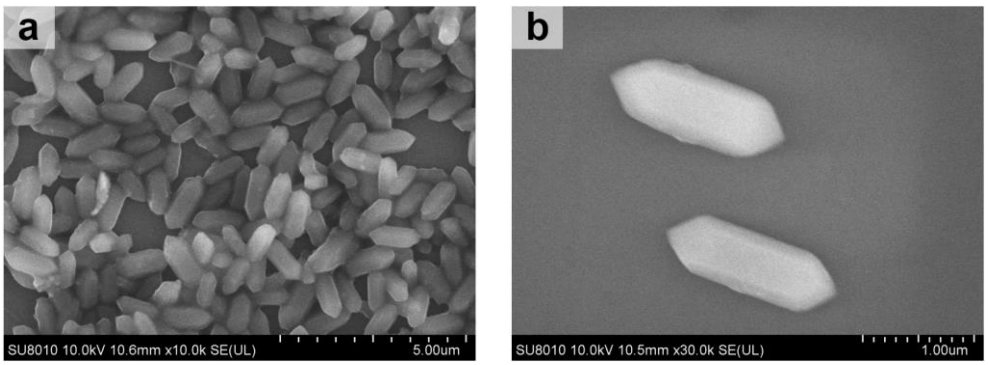

Figure S1. SEM images of pristine **1a** sample with (a) low magnification and (b) high magnification.

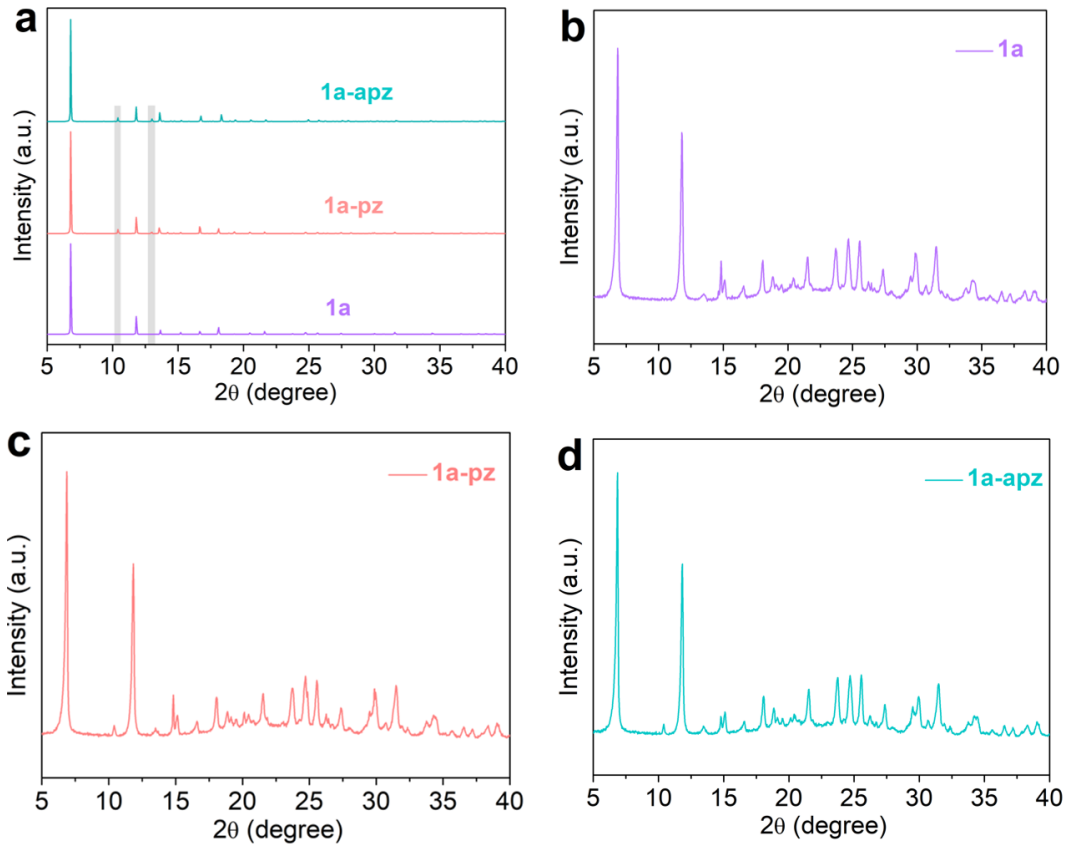

Figure S2. (a) Theoretical PXRD patterns of **1a**, **1a-pz**, and **1a-apz**, respectively; (b-d) corresponding powder PXRD patterns of as-synthesized samples.

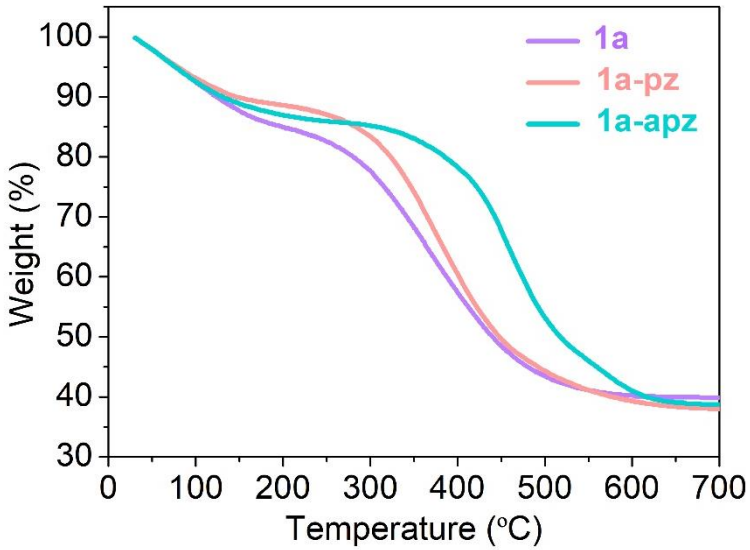

Figure S3. Thermogravimetric analysis (TGA) curves of the as-synthesized samples.

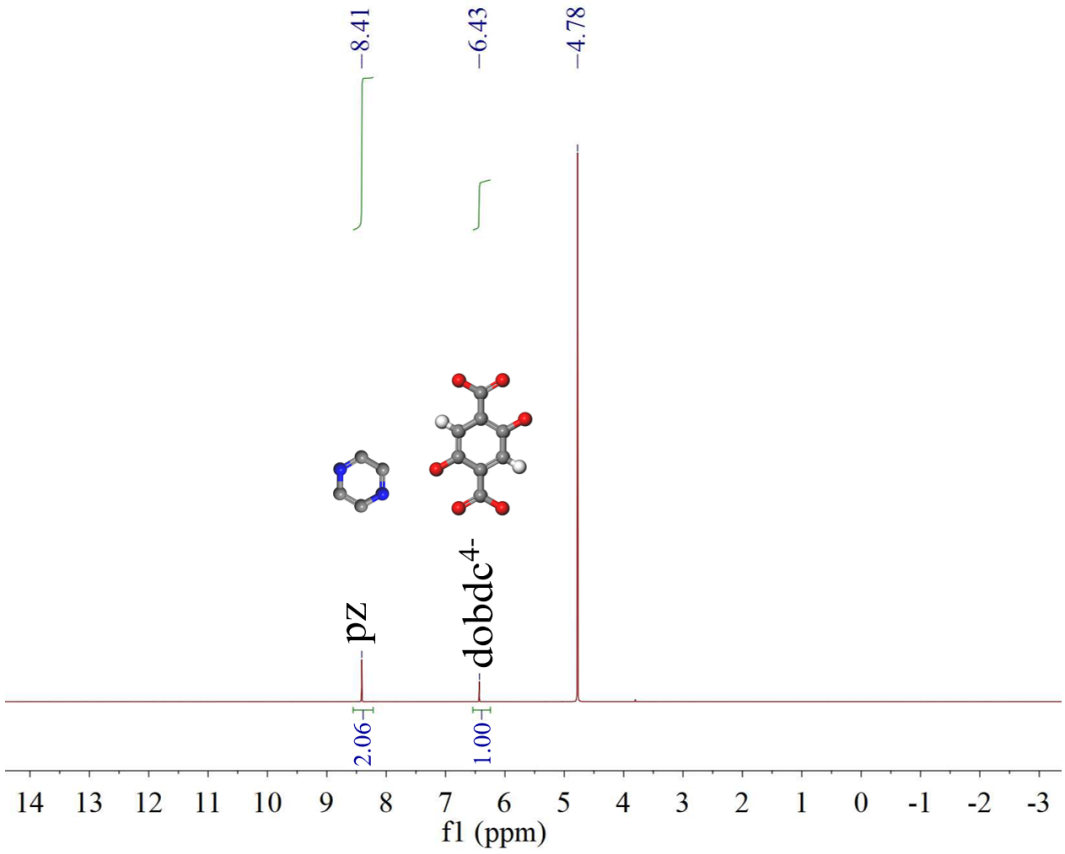

Figure S4. ^{1}H NMR spectrum of **1a-pz** digested in 1 M $NaOH/D_2O$ for 24 h.

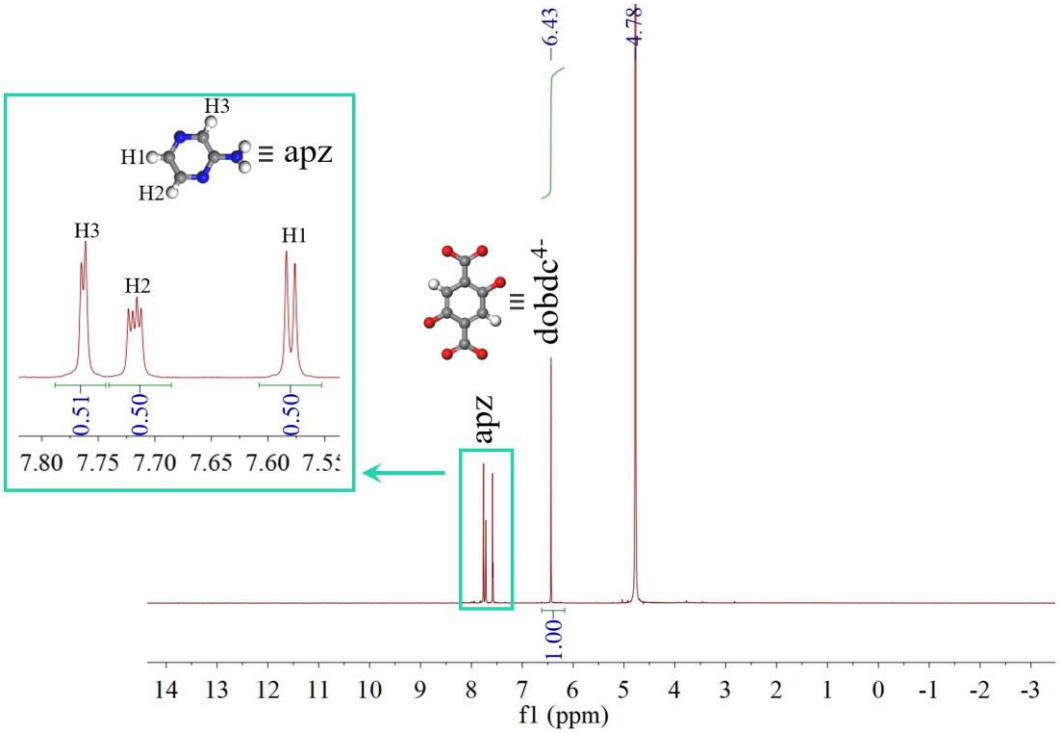

Figure S5. ^{1}H NMR spectrum of **1a-apz** digested in 1 M NaOH/D_2O for 24 h.

Note: The H attached to the amino group of apz may undergo proton exchange with the solvent or react with NaOH, resulting in no peaks.

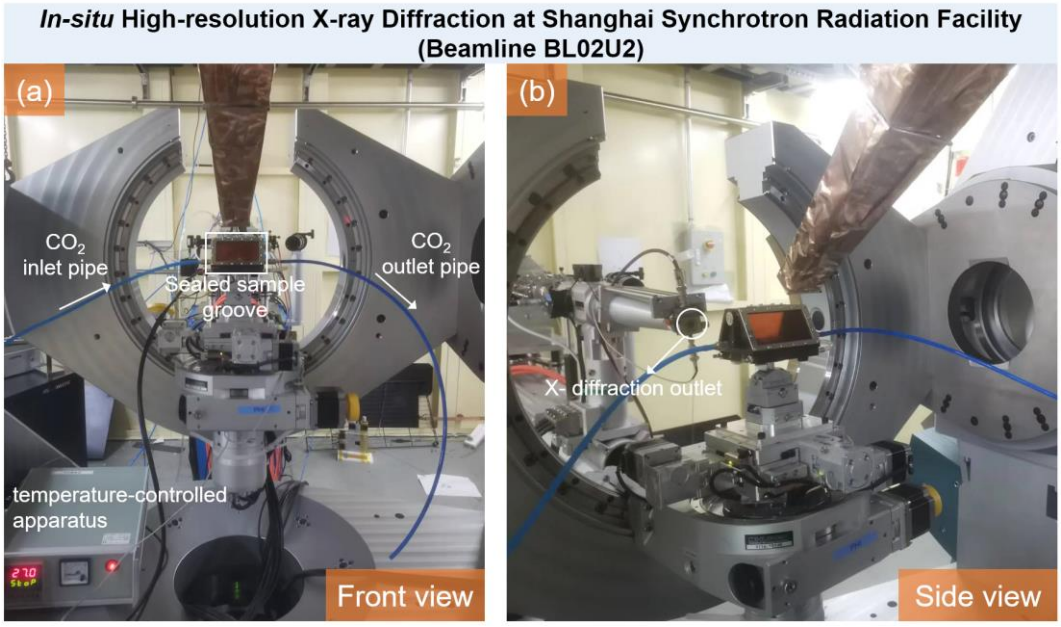

Figure S6. Setup for the *in-situ* high-resolution synchrotron X-ray diffraction (HR-SXRD) tests: (a) front view, (b) side view.

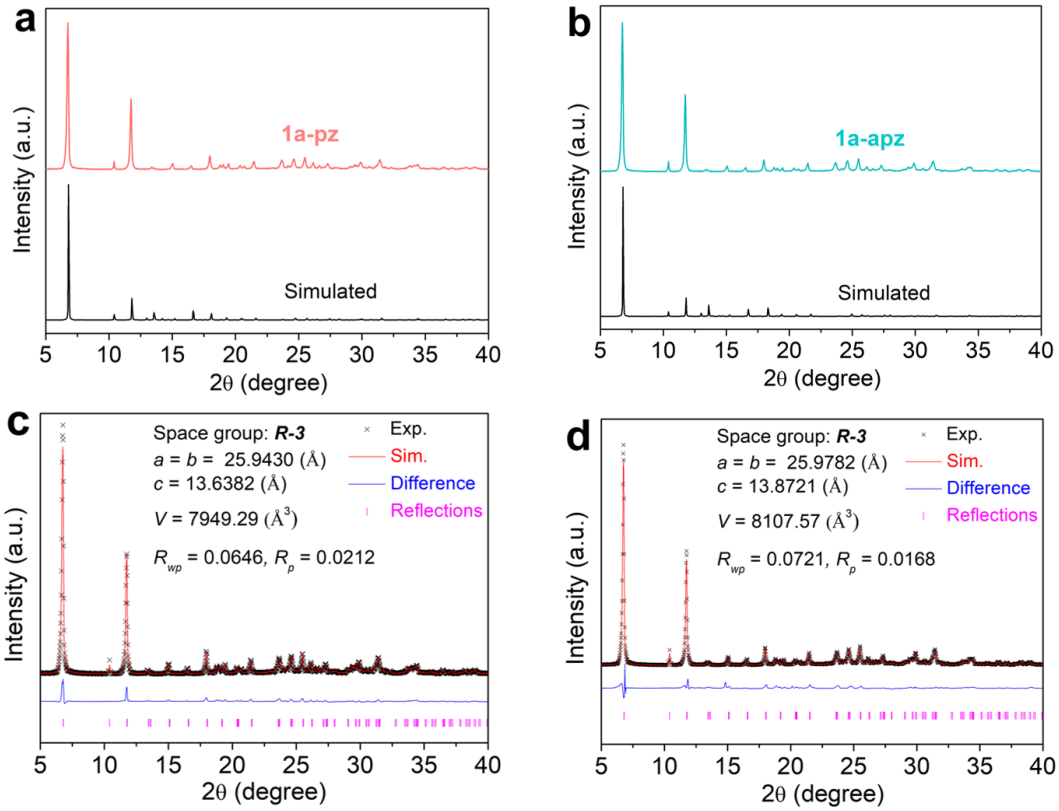

Figure S7. Experimental HR-SXRD of (a) **1a-pz** and (b) **1a-apz**; Rietveld refinements on HR-SXRD data of (c) **1a-pz** and (d) **1a-apz** collected at room temperature.

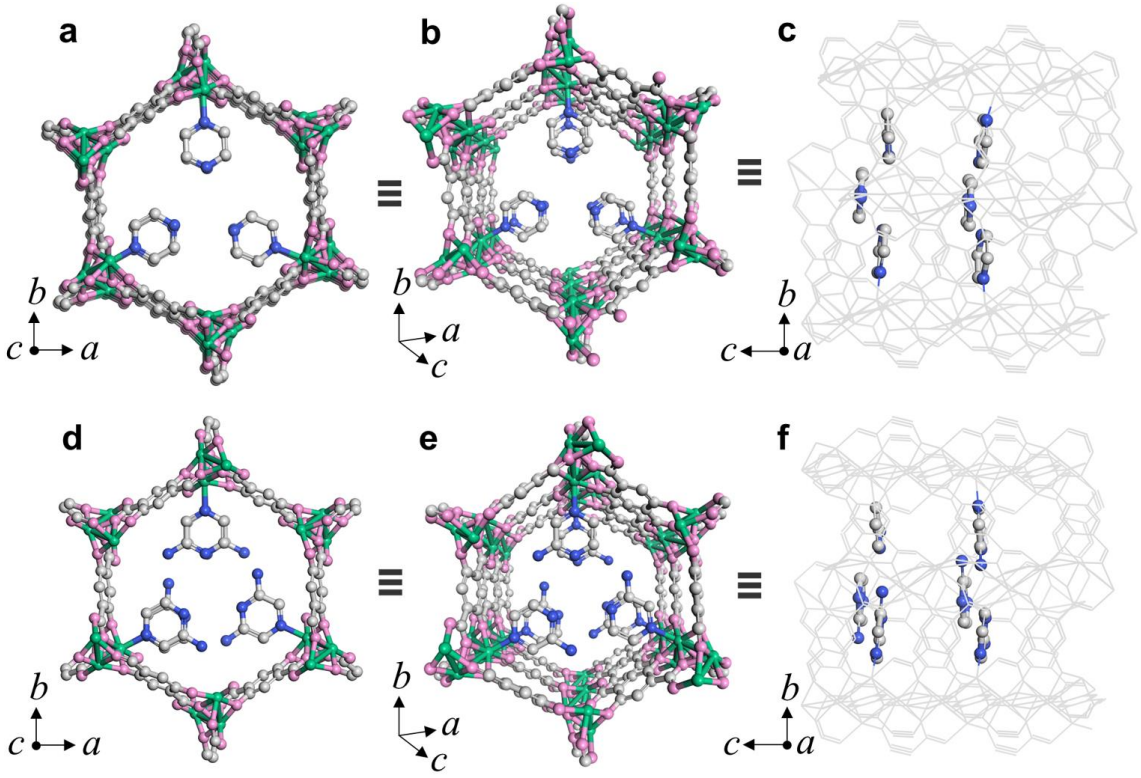

Figure S8. Spatial position of pz in local **1a** topology in (a) orthographic, (b) perspective, and (c) side view after Rietveld refinements; Spatial position of apz in local **1a** topology in (d) orthographic, (e) perspective, and (f) side view after Rietveld refinements.

Note: All the structures were resolved from the HR-SXRD data.

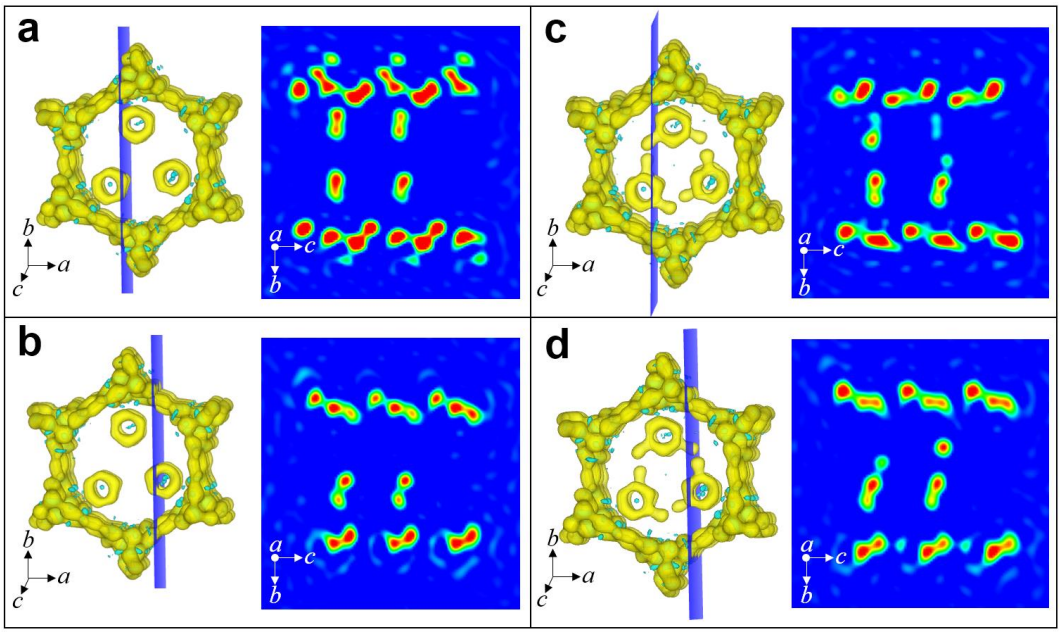

Figure S9. The electron density maps obtained from Fourier transformation of the density difference between observed HR-SXRD reflections and calculated reflections: (a-b) The electron diffraction spots projected by **1a-pz** in different lattice plane positions with the same Miller indices of (100); (c-d) The electron diffraction spots projected by **1a-apz** in different lattice plane positions with the same Miller indices of (100).

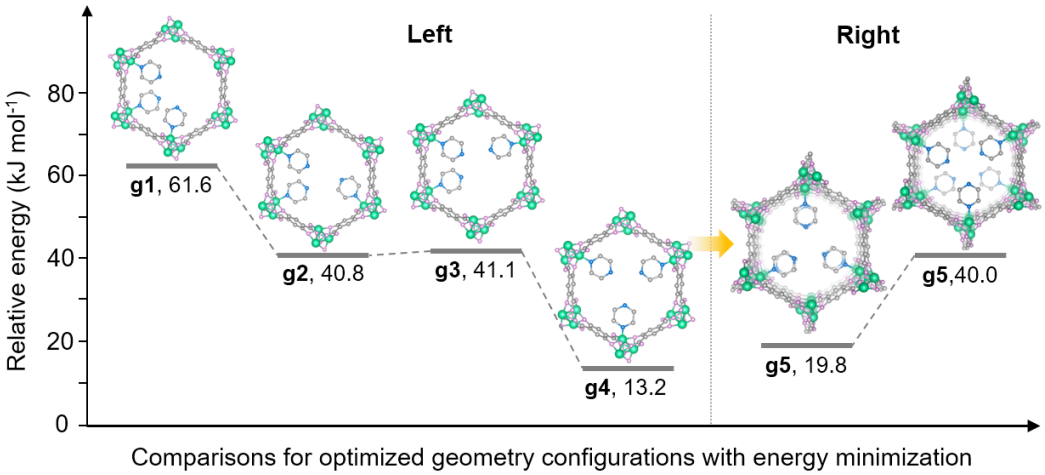

Figure S10. Comparisons for optimized geometry locations with energy minimization for **1a-pz**.

Note: **Left** and **Right** areas represent the modeling optimization with one layer or two layers of pz in the pore. **Right** structures were modeled based on **g4** model with lowest energy (13.2 kJ mol^{-1}). Obviously, the structure with two layers exhibited lowest steady-state energy of 19.8 kJ mol^{-1} and could be used as the initial full structure for subsequent analysis.

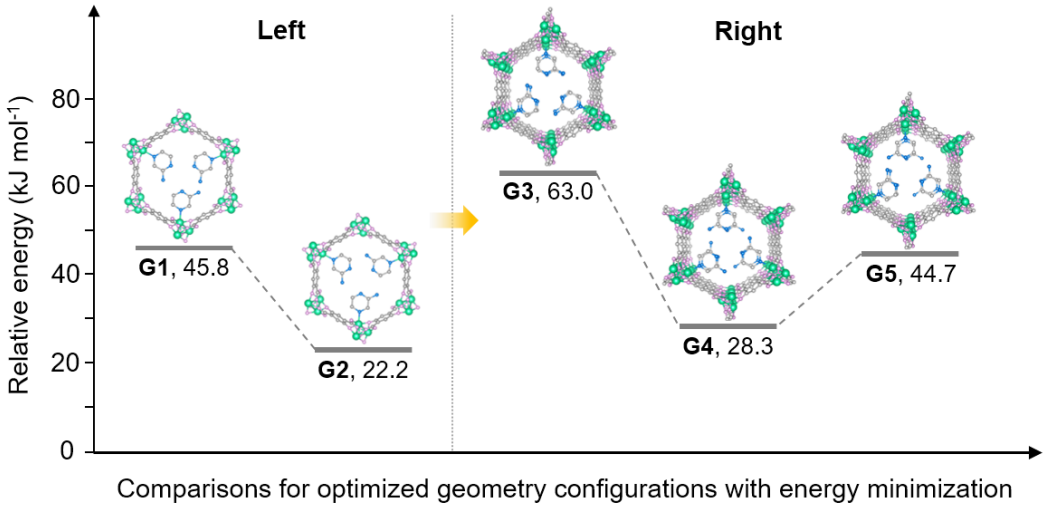

Figure S11. Comparisons for optimized geometry locations with energy minimization for **1a-apz**.

Note: **Left** and **Right** areas represent the modeling optimization with one layer or two layers of apz in the pore. **Right** structures were modeled based on **G2** model with lowest energy (22.2 kJ mol^{-1}). Obviously, the structure with two layers exhibited lowest steady-state energy of 28.3 kJ mol^{-1} and could be used as the initial full structure for subsequent analysis.

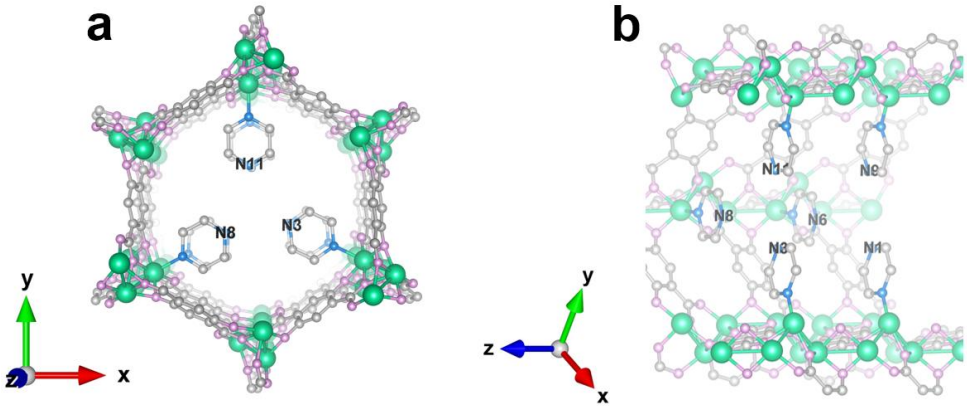

Figure S12. (a) Crystallographic view of **1a-pz** after structural optimization along crystallographic *z*-axis; (b) Side view of **1a-pz**, showing the spatial locations of pz motif in the pore.

Note: N atoms attached to pz were marked with light blue, and all H atoms were omitted for clarity.

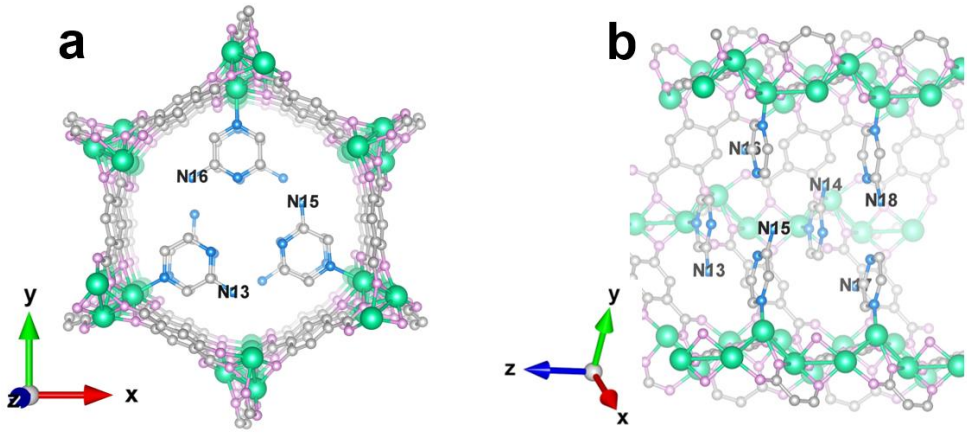

Figure S13. (a) Crystallographic view of **1a-apz** after structural optimization along crystallographic *z*-axis; (b) Side view of **1a-apz**, showing the spatial locations of apz motif in the pore.

Note: N atoms attached to apz were marked with light blue, and all H atoms were omitted for clarity.

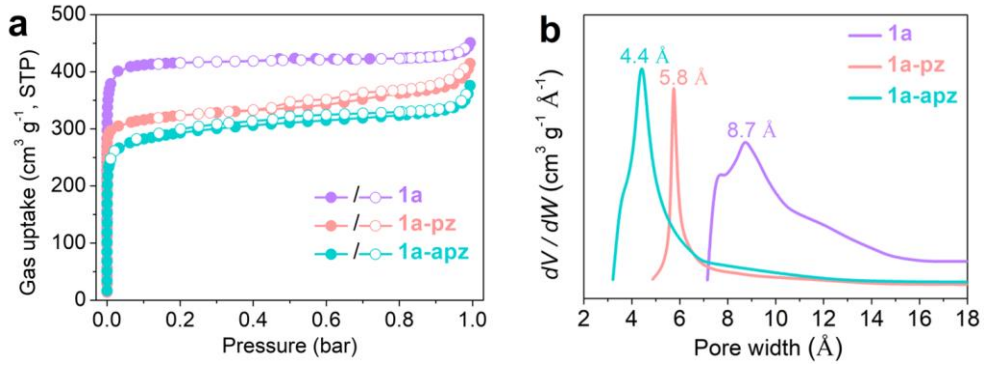

Figure S14. (a) N_2 sorption isotherms at 77 K and 1 bar (filled, adsorption; open, desorption); (b) Pore size distribution based on the microporous Horvath–Kawazoe model.

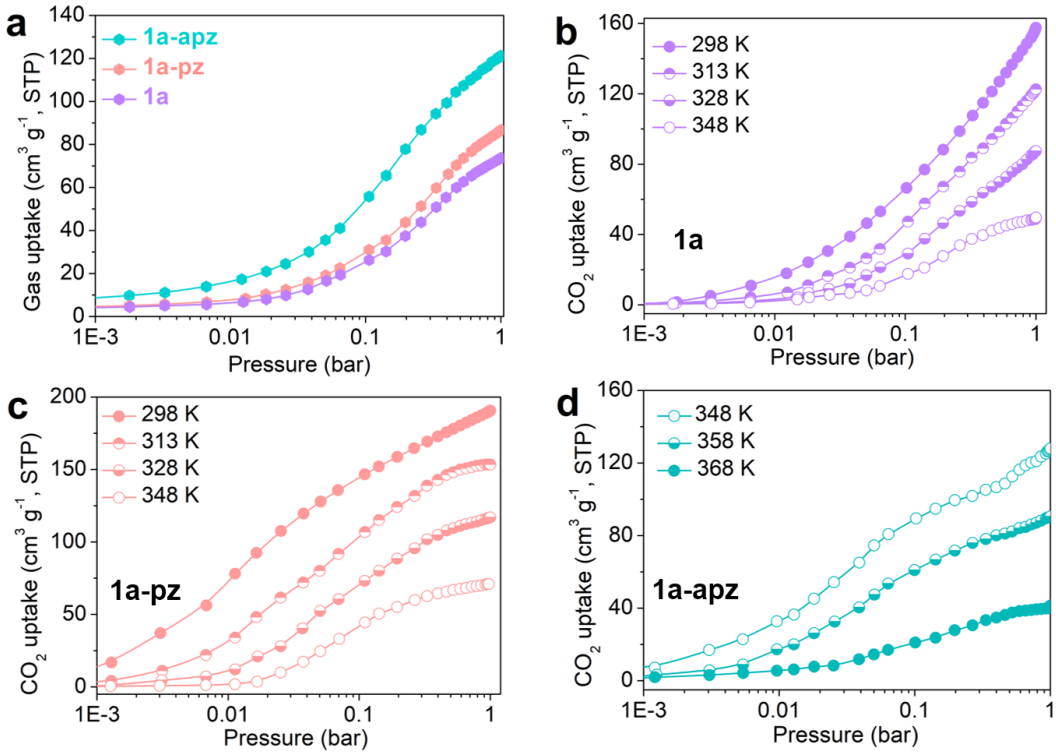

Figure S15. (a) Adsorption isotherms of CO on various samples at 298 K; Adsorption isotherms of CO_2 on (b) **1a**, (c) **1a-pz,** and (d) **1a-apz** at variable temperatures.

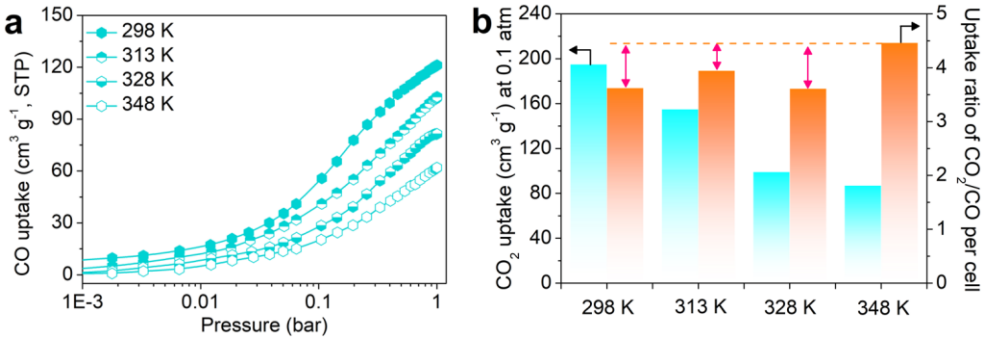

Figure S16. Adsorption isotherm of CO on **1a-apz** at variable temperatures; (b) Comparisons of CO_2 uptake at 0.1 atm and uptake ratio of CO_2/CO per unit cell at variable temperatures.

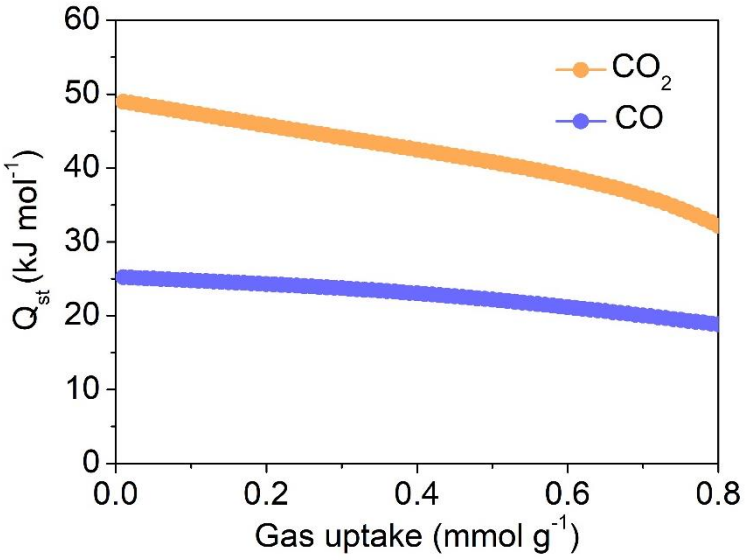

Figure S17. Coverage-dependent adsorption heat profiles of guest molecules on **1a-apz** obtained by the virial fitting method.

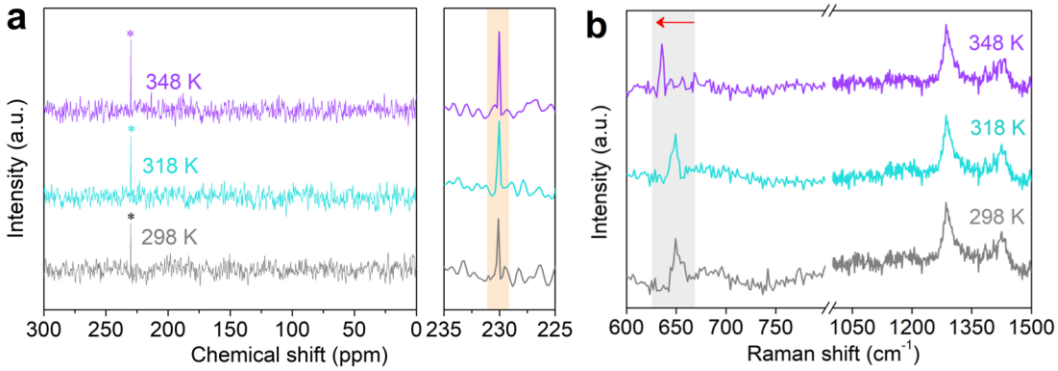

Figure S18. (a) Variable-temperature-dependent CP-MAS ^{15}N solid-state NMR spectra of **1a-pz**; (b) *In-situ* variable-temperature-dependent Raman spectra of **1a-apz**.

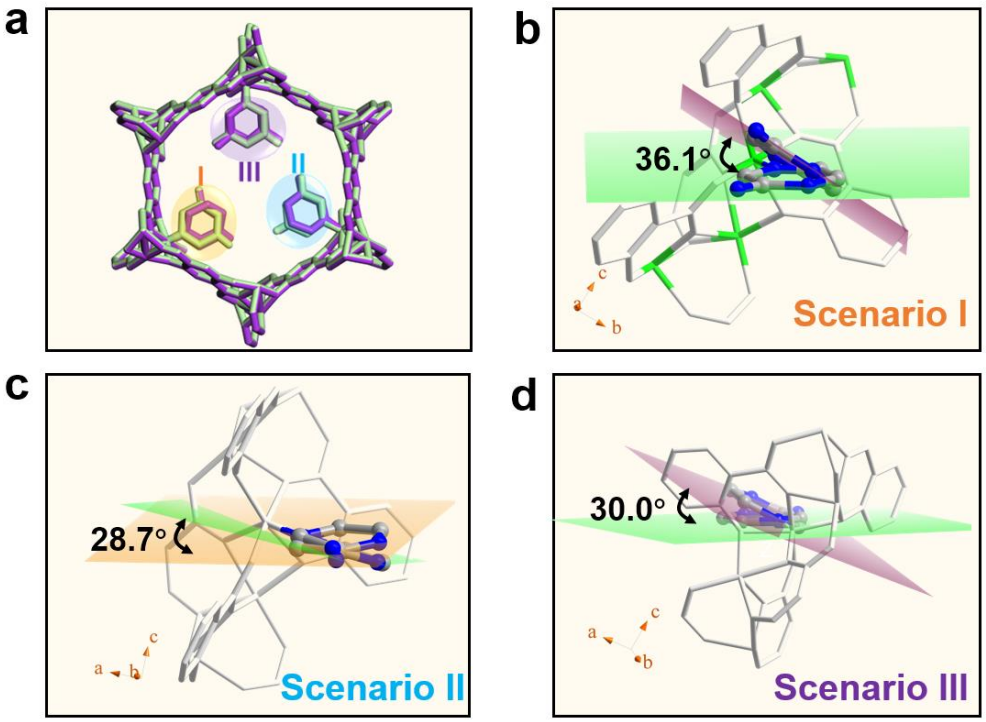

Figure S19. (a) Comparisons of the steady-state geometry conformation with lowest energies for **1a-apz** at 298 K (colored with lavender) and 348 K (colored with green); (b-d) Enlarged perspectives of staggered conformations scenarios in (a).

Note: C and N atoms in apz were colored with gray-50% and blue, respectively; other atoms were colored with white for clarity.

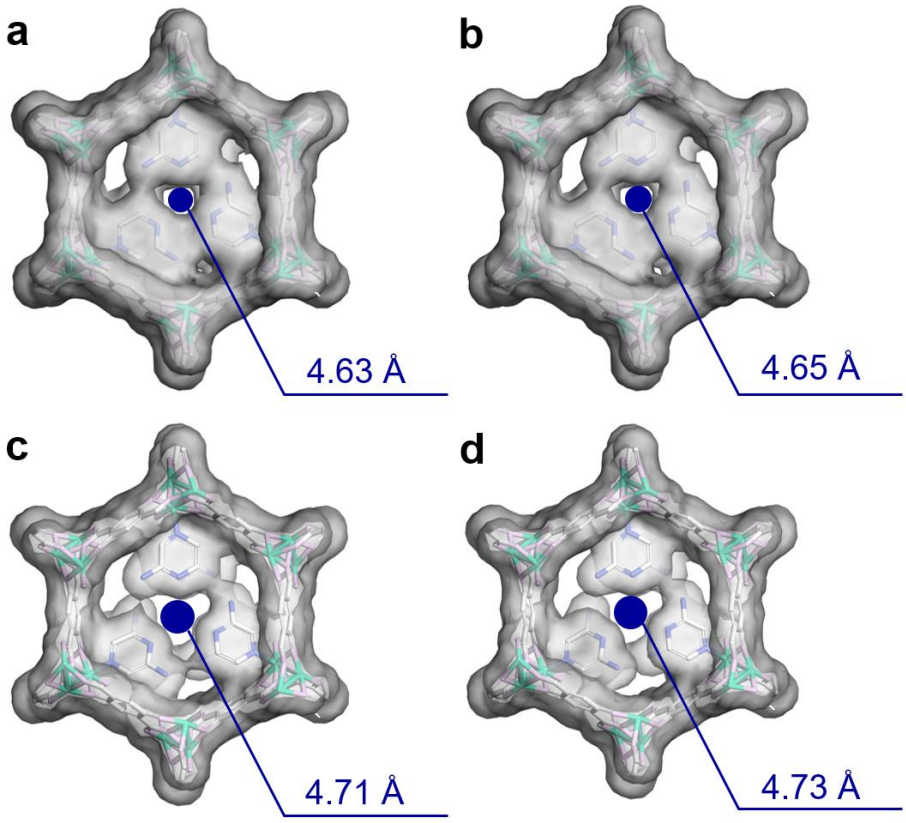

Figure S20. Pore evolution of CO_2⊂**1a-apz** upon pressure-dependent CO_2 adsorption process, with (a) 10, (b) 25, (c) 50, and (d) 100 mbar of CO_2 in **1a-apz** by removing the guests from the steady-state adsorption conformation and analyzing the remaining pore space with a Connolly radius of 1.1 Å.

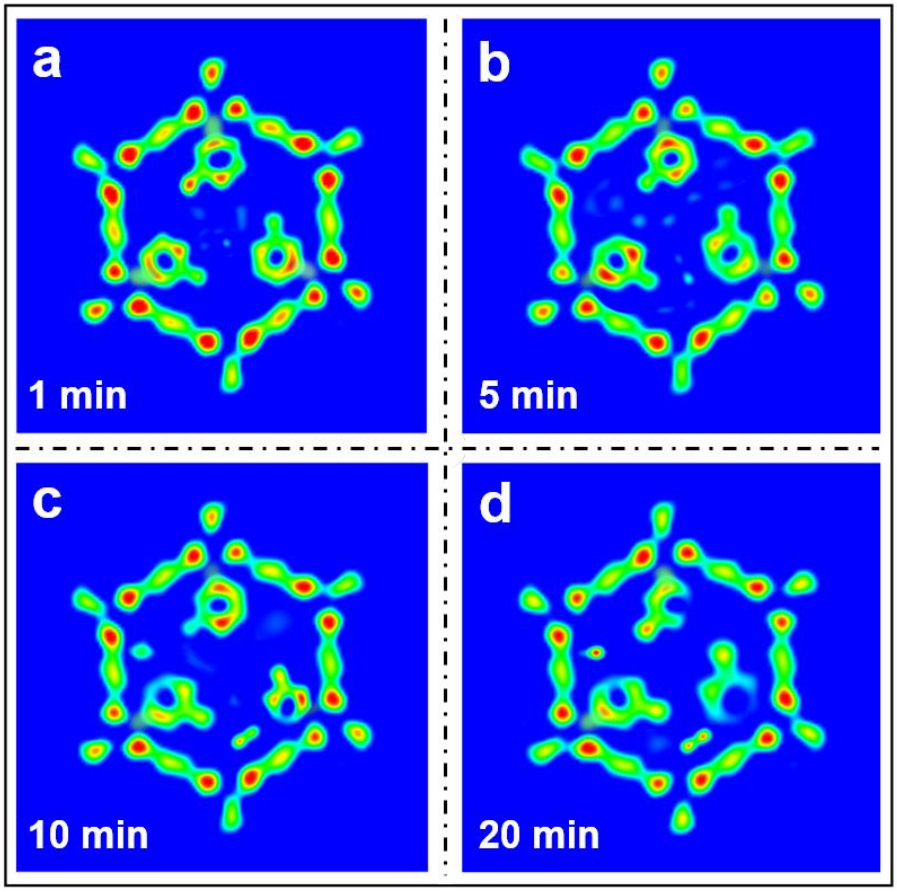

Figure S21. Transient two-dimensional electron-density maps (2D-EDM) yielded from transient PXRD files of CO_2⊂**1a-apz** under a CO_2 pressure of 0.1 bar at 348 K: (a) 1 min; (b) 5 min; (c) 10 min; (d) 20 min.

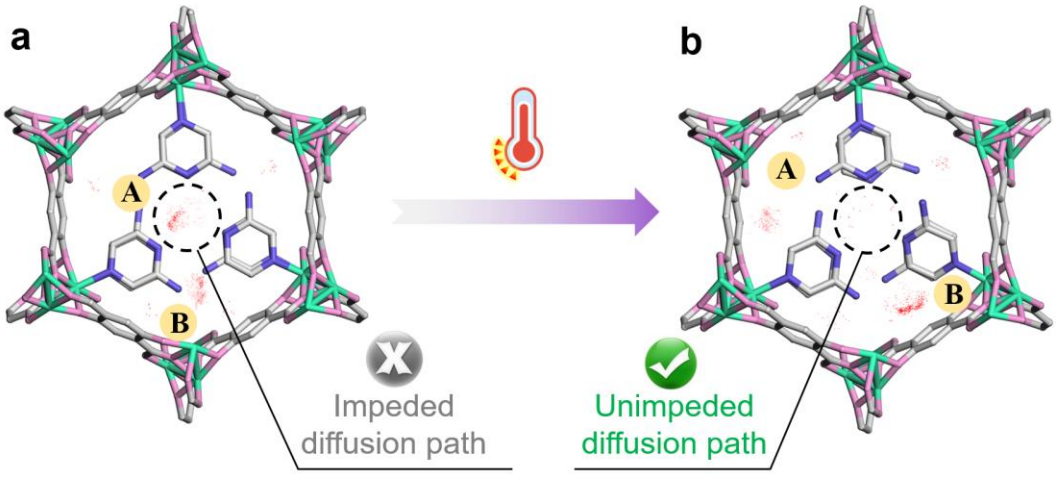

Figure S22. Density distribution of CO_2 molecules within **1a-apz** obtained from GCMC simulation.

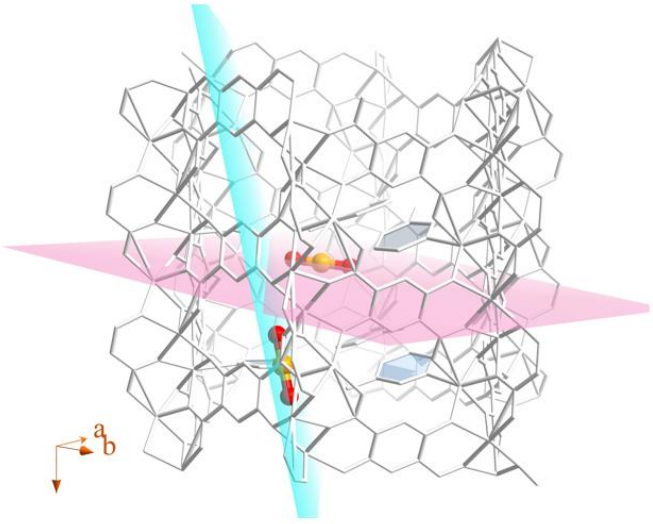

Figure S23. Visualized planes of guest molecules yielded from DFT-calculated binding sites.

Note: Oxygen and carbon atoms in guest CO_2 are highlighted with red and orange, respectively; other atoms in the MOF structure are highlighted with white for clarity.

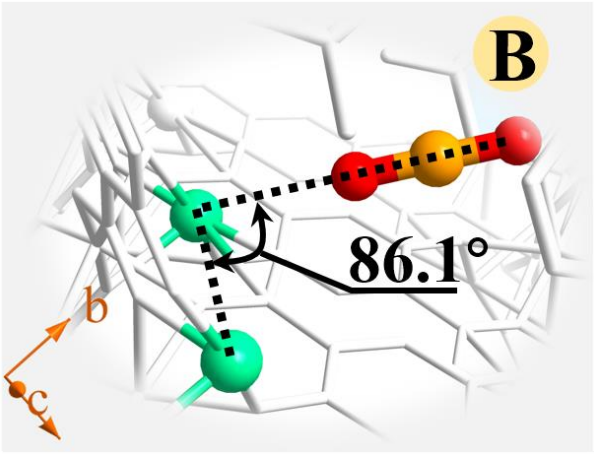

Figure S24. Enlarged perspective of the binding conformation for CO_2⊂**1a-apz**, showing the tilted angle of 86.1° between linear CO_2 and *c*-axis dimension at **Site B**.

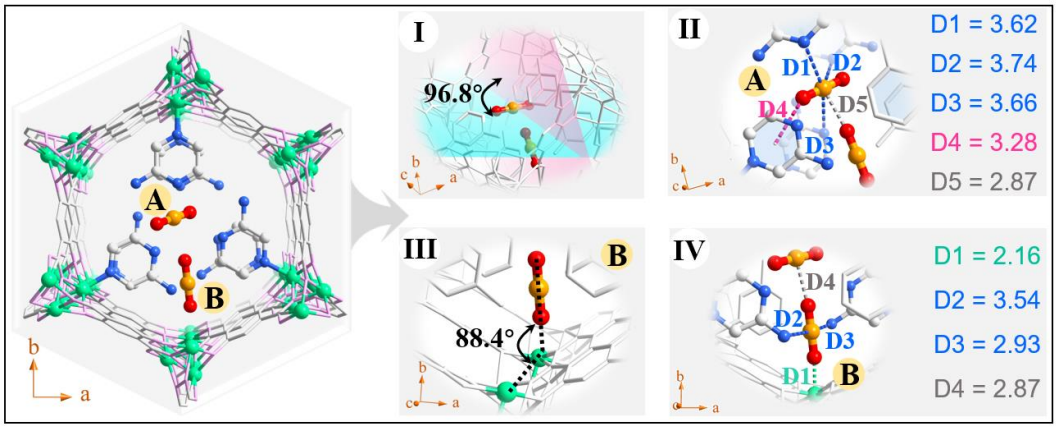

Figure S25. DFT-calculated adsorption conformation of CO_2-loaded **1a-apz** at 298 K.

Note: The bond length is calculated based on average statistics to maximum eliminate possible errors; the binding types colored with green, blue, pink, and gray refer to π-complexation effect, Lewis acid/base interactions, van der Waals interactions, and intramolecular forces, respectively. Here the bond lengths are in angstroms. Color modes: Mg, green; O, light pink; N, blue; C, gray-25%; all H atoms were omitted for clarity.

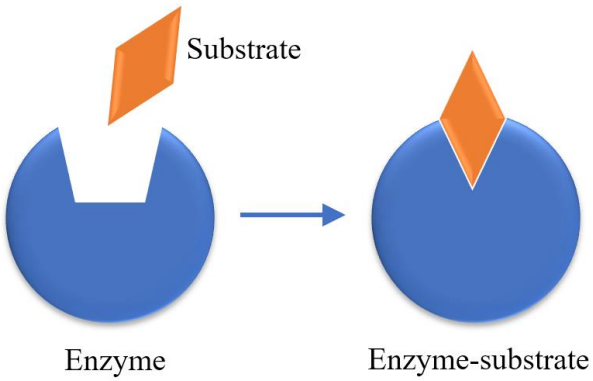

Figure S26. Illustration of the induced-fit-identification mechanism in substrate-enzyme binding.

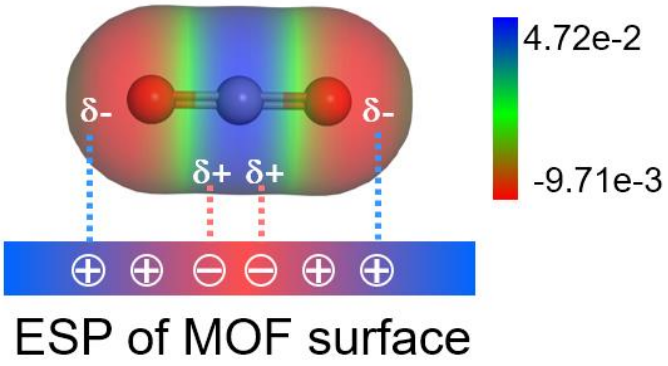

Figure S27. Binding interaction between MOF surface and CO_2 molecule through complementary electrostatic potential (ESP) effect.

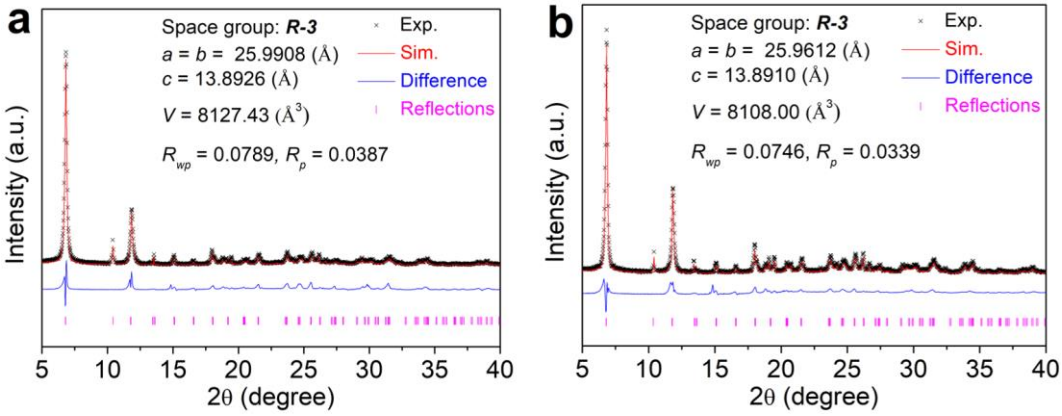

Figure S28. *In-situ* HR-SXRD experiments and Rietveld structural refinements for CO_2-loaded **1a-apz** at (a) 298 K and (b) 348 K.

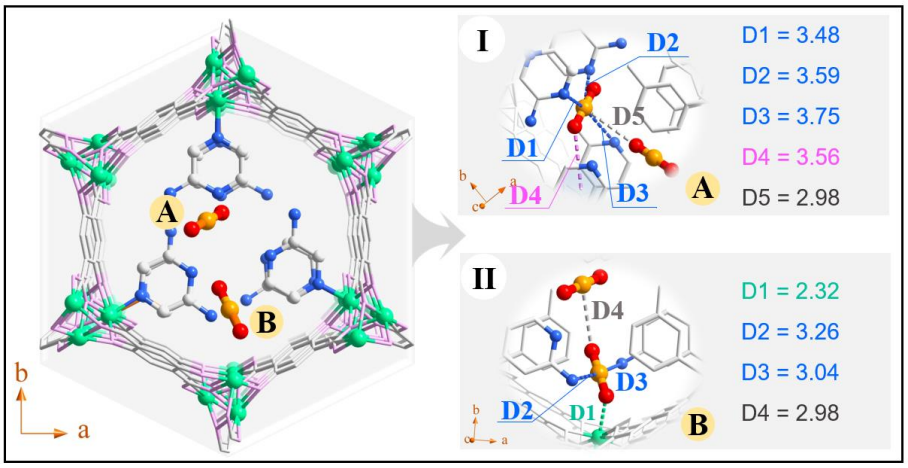

Figure S29. The adsorption conformation of CO_2-loaded **1a-apz** at 298 K were yielded from Rietveld refinements of *in-situ* HR-SXRD data and further structural optimization using DFT method.

Note: The bond length is calculated based on average statistics to maximum eliminate possible errors; the binding types colored with green, blue, pink, and gray refer to π-complexation effect, Lewis acid/base interactions, van der Waals interactions, and intramolecular forces, respectively. Here the bond lengths are in angstroms. Color modes: Mg, green; O, light pink; N, blue; C, gray-25%; all H atoms were omitted for clarity.

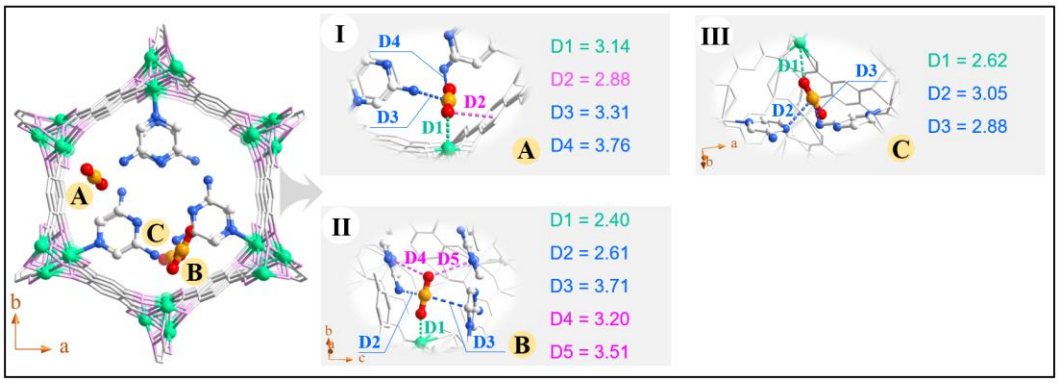

Figure S30. The adsorption conformation of CO_2-loaded **1a-apz** at 348 K were yielded from Rietveld refinements of *in-situ* HR-SXRD data and further structural optimization using DFT method.

Note: The bond length is calculated based on average statistics to maximum eliminate possible errors; The binding types colored with green, blue, and pink refer to π-complexation effect, Lewis acid/base interactions, and van der Waals interactions, respectively. Here the bond lengths are in angstroms. Color modes: Mg, green; O, light pink; N, blue; C; all H atoms were omitted for clarity.

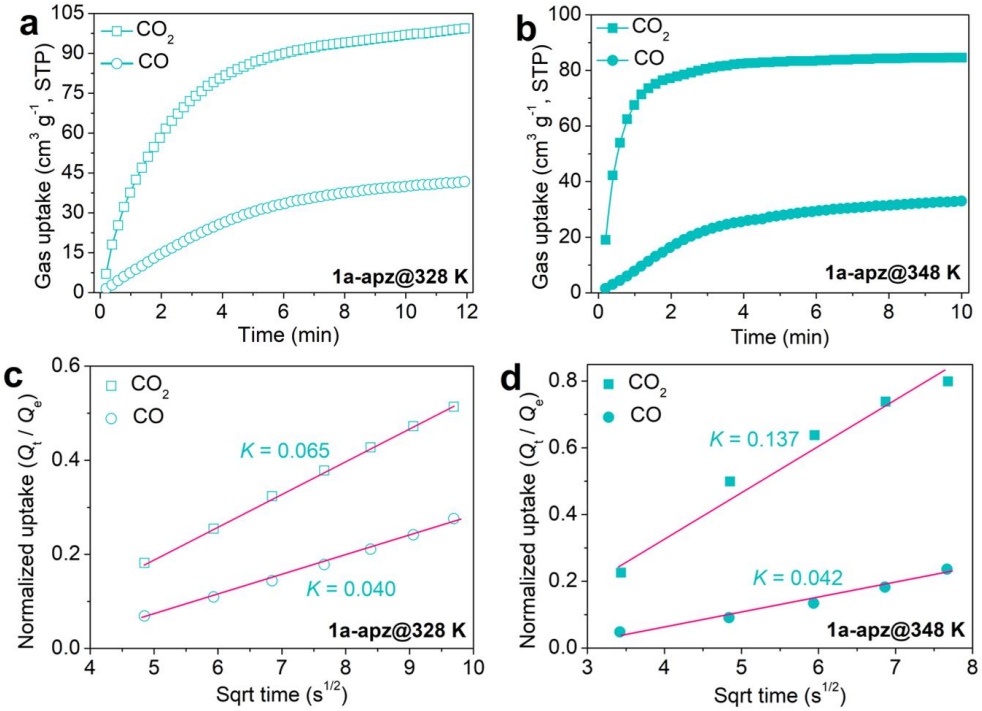

Figure S31. (a-b) Kinetic adsorption files of CO_2 and CO for **1a-apz** at 328 and 348 K, respectively; (c-d) Normalized Q_t/Q_e against $s^{1/2}$ at 328 and 348 K, respectively.

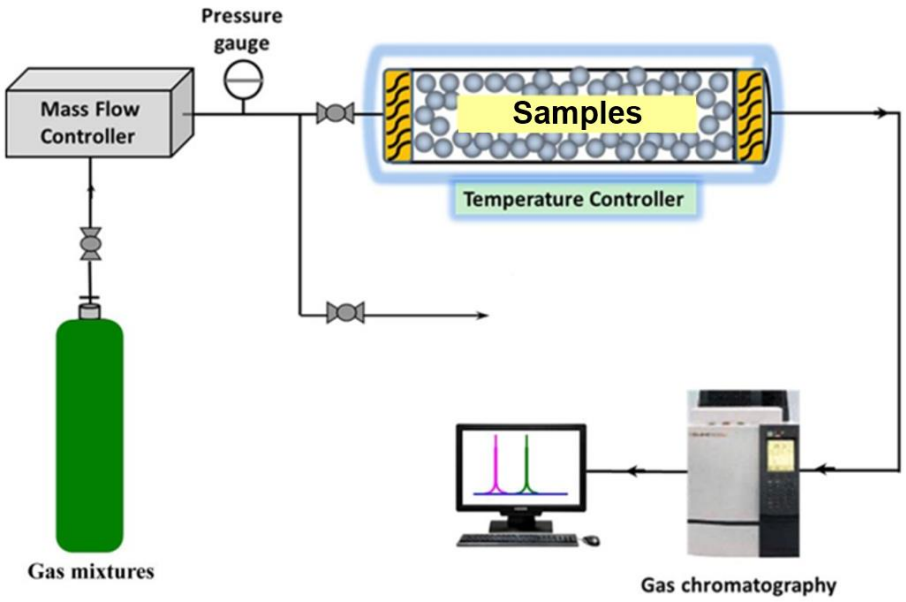

Figure S32. Schematic illustration of the apparatus for the breakthrough tests.

Supplementary Tables

Table S1. Elemental analysis (EA) and ICP analysis of elements in yielding MOFs.

MOFs	Experimental content[a] (wt. %; mmol)					Molar ratio of elements (experimental value[b]; theoretical value[c])			
	C	H	O	N	Mg	C/Mg	H/Mg	O/Mg	N/Mg
1a	15.0; 4.66	0.3; 1.12	14.0; 3.26	0;0	7.7; 1.18	3.95;4	0.95;1	2.76;3	0;0
1a-pz	11.0; 3.42	0.5; 1.87	7.6; 1.77	2.1; 0.56	3.8; 0.58	5.90;6	3.22;3	3.05;3	0.97;1
1a-apz	10.6; 3.29	0.5; 1.87	7.0; 1.63	3.1; 0.83	3.6; 0.55	5.98;6	3.40; 3.5	2.96;3	1.50;1.5

[a] The actual amount contents of elements in the yielding MOFs.

[b] The calculated molar ratio of elements in the MOFs through experimental methods.

[c] The theoretical molar ratio of elements in the MOFs, given the unit formula of $[Mg_2(dobdc)(pz)]$ or $[Mg_2(dobdc)(apz)]$.

Table S2. Crystallographic parameters of **1a-pz** and **1a-apz** obtained from Rietveld refinements of HR-SXRD data and further structural optimization using DFT method.

Samples	**1a-pz**	**1a-apz**
Temperature / K	298	298
Radiation type	Synchrotron	Synchrotron
Diffractometer	beamline BL02U2	beamline BL02U2
Data collection mode	Transmission	Transmission
Formula	$C_{12}H_6N_2O_6Mg_2$	$C_{12}H_{6.88}N_3O_6Mg_2$
Formula weight	322.6	337.5
Crystal system	Hexagonal	Hexagonal
Space group	***R-3***	***R-3***
$a = b$ (Å)	25.9430	25.9782
c (Å)	13.6382	13.8721
α (°)	90	90
β (°)	90	90
γ (°)	120	120
cell volume (Å^3)	7949.29	8107.57
Density (g cm^{-3})	1.21	1.25
Z	18	18
R_P (%)	2.12	1.68
R_{WP} (%)	6.46	7.21
GOF	1.57	1.17
CCDC	2264297	2264296

Table S3. Binding configurations and distances between pz motif and framework yielded from molecular simulations and HR-SXRD Rietveld structural refinements.

Binding configuration	Distance[a] (Å)	Distance[b] (Å)	Relative error[c] (%)
Mg(38)-N(7)	2.09	2.17	3.83
Mg(50)-N(4)	2.10	2.02	3.81
Mg(45)-N(12)	2.10	2.11	0.48
Mg(32)-N(2)	2.11	2.18	3.32
Mg(20)-N(5)	2.10	2.21	5.24
Mg(27)-N(10)	2.09	2	4.31
N(1)···N(9)	4.50	4.32	4.00
N(1)···N(6)	4.29	4.33	0.93
N(6)···N(9)	4.83	4.81	0.41
N(8)···N(11)	4.67	4.77	2.14
N(3)···N(11)	4.61	4.5	2.39
N(3)···N(8)	4.33	4.45	2.77

[a] The distances were obtained from molecular simulations.

[b] The distances were obtained from experimental Rietveld structural refinements.

[c] The relative error (absolute value) was calculated based on $[\frac{\text{Distance}^b-\text{Distance}^a}{\text{Distance}^a}]\times 100\%$

Table S4. Binding configurations and distances between apz motif and framework yielded from molecular simulations and HR-SXRD Rietveld structural refinements.

Binding configuration	Distance[a] (Å)	Distance[b] (Å)	Relative error[c] (%)
Mg(38)-N(7)	2.15	2.12	1.40
Mg(50)-N(4)	2.15	2.26	5.12
Mg(45)-N(12)	2.14	2.12	0.93
Mg(32)-N(2)	2.15	2.18	1.40
Mg(20)-N(5)	2.16	2.15	0.46
Mg(27)-N(10)	2.15	2.17	0.93
N(13)···N(15)	6.59	6.48	1.67
N(15)···N(16)	6.46	6.40	0.93
N(13)···N(16)	7.08	6.61	6.64
N(14)···N(17)	6.62	6.51	1.66
N(14)···N(18)	6.60	6.66	0.91
N(18)···N(17)	6.34	6.30	0.63

[a] The distances were obtained from molecular simulations.

[b] The distances were obtained from experimental Rietveld structural refinements.

[c] The relative error (absolute value) was calculated based on $[\frac{Distance^b - Distance^a}{Distance^a}] \times 100\%$

Table S5. The parameters of virial equation for CO_2 and CO on **1a-apz**.

Gas	a_0	a_1	a_2	a_3	a_4	a_5	a_6	a_7	b_0	b_1	b_2
CO_2	-5909	2001	288	-1206	766	1184	-1662	2886	11.1	0.23	-0.049
CO	-3038	601	-399	1886	-1663	2408	-2886	1108	8.1	0.91	-0.081

Table S6. A detailed comparison of the "induced-fit" binding mechanism in the literature and this work.

Reported induced-fit mechanism	Ref.
induced-fit transformations step by step, including **deformation/reconstruction of channels, contraction of pores, and reconstruction of active sites**	[9]
induced-fit effect is realized **through the cooperative action of open metal sites**	[10]
Induced-fit mechanism originated from **i) degree of freedom in the structure and electronic structure; ii) multiple hydrogen bonding interactions; iii) rotational motion of the pillar and organic ligand**	[11]
Induced-fit mechanism is formed through **specific interactions with the guests**	[12]
The **flexibility results from the framework adapting aptly with increased temperature** to produce species-specific induced-fits	[13]
This induced fit is attributed to **isomerisation from square pyramidal to square planar geometry**	[14]
the **structural deformation** greatly facilitated further n-butanol adsorption, which we defined as the "Induced-Fit Suction" (IFS) effect	[15]
which could act as **reliable coordination sites**, offer an effective guarantee to MA-TMA for the separation of uranyl in situ in the induced fit mode	[16]
the unique mechanism in our work is mainly attributed to the synergistic effects, comprising **self-adaptive behavior of apz motif, multiple binding sites, and unusual electrostatic potential reconfiguration**	**This work**

Table S7. Crystallographic parameters of CO_2-loaded **1a-apz** obtained from Rietveld refinements of HR-SXRD data and further structural optimization using DFT method.

Samples	CO_2⊂**1a-apz**	CO_2⊂**1a-apz**
Temperature/K	298	348
Radiation type	Synchrotron	Synchrotron
Diffractometer	beamline BL02U2	beamline BL02U2
Data collection mode	Transmission	Transmission
Formula	$C_{12}H_{6.88}N_3O_6Mg_2 \cdot 1.33CO_2$	$C_{12}H_{6.88}N_3O_6Mg_2 \cdot 0.66CO_2$
Formula weight	396.0	366.5
Crystal system	Hexagonal	Hexagonal
Space group	***R-3***	***R-3***
$a = b$ (Å)	25.9908	25.9612
c (Å)	13.8926	13.8910
α (°)	90	90
β (°)	90	90
γ (°)	120	120
cell volume (Å^3)	8127.43	8108.00
Density (g cm^{-3})	1.46	1.35
Z	18	18
R_P (%)	3.87	3.39
R_{WP} (%)	7.89	7.46
GOF	2.12	1.85
CCDC	2264298	2264299

Table S8. Dual-site Langmuir-Freundlich parameters fit for CO_2 and CO on **1a-pz** and **1a-apz** at 298 K.

		Site A			**Site B**		
		N_1	*a*	*b*	N_2	*c*	*d*
		mol kg^{-1}	Pa^{-vA}	dimensionless	mol kg^{-1}	Pa^{-vA}	dimensionless
1a-pz	CO_2	5.217	0.312	0.4108	1.741	2.217	0.618
	CO	0.301	1.119	2.941	1.171	2.001	2.000
1a-apz	CO_2	7.400	0.2011	0.1015	1.8041	2.1196	0.4161
	CO	2.712	2.151	1.122	1.4108	1.2205	1.8109

References

[1] P. Hu, H. Liu, H. Wang, J. Zhou, Y. Wang, H. Ji, *J. Mater. Chem. A* **2022**, *10*, 881-890.

[2] D. Sun, G. Sun, X. Zhu, F. Ye, J. Xu, *Fuel* **2018**, *211*, 609-620.

[3] J. P. Perdew, K. Burke, M. Ernzerhof, *Phys. Rev. Lett.* **1996**, *77*, 3865.

[4] M. Zhang, X. Huang, Y. Chen, *Phys. Chem. Chem. Phys.* **2016**, *18*, 28854-28863.

[5] a) R. Krishna, *Micropor. Mesopor. Mat.* **2014**, *185*, 30-50; b) R. Krishna, *RSC Adv.* **2015**, *5*, 52269-52295; c) R. Krishna, *RSC Adv.* **2017**, *7*, 35724-35737.

[6] M. J. J. Frisch, Gaussian 03 Rev. E. 01. **2004**.

[7] S. Ehrlich, J. Moellmann, W. Reckien, T. Bredow, S. Grimme, *ChemPhysChem* **2011**, *12*, 3414-3420.

[8] P. Hu, H. Wang, C. Xiong, H. Liu, J. Han, J. Zhou, Z. Zhao, Y. Wang, H. Ji, *ACS Sustain. Chem. & Eng.* **2021**, *9*, 15897-15907.

[9] J. Tian, Q. Chen, F. Jiang, D. Yuan, M. Hong, *Angew. Chem. Int. Ed.* **2023,** *62*, e202215253.

[10] H. Zeng, M. Xie, Y. L. Huang, Y. Zhao, X. J. Xie, J. P. Bai, M. Y. Wan, R. Krishna, W. Lu, D. Li, *Angew. Chem. Int. Ed.* **2019**, *58*, 8515-8519.

[11] M. Shivanna, K. I. Otake, B. Q. Song, L. M. van Wyk, Q. Y. Yang, N. Kumar, W. K. Feldmann, T. Pham, S. Suepaul, B. Space, L. J. Barbour, S. Kitagawa, M. J. Zaworotko, *Angew. Chem. Int. Ed.* **2021**, *60*, 20383-20390.

[12] A. P. Katsoulidis, D. Antypov, G. F. S. Whitehead, E. J. Carrington, D. J. Adams, N. G. Berry, G. R. Darling, M. S. Dyer, M. J. Rosseinsky, *Nature* **2019**, *565*, 213-217.

[13] M. H. Yu, B. Space, D. Franz, W. Zhou, C. He, L. Li, R. Krishna, Z. Chang, W. Li, T. L. Hu, X. H. Bu, *J. Am. Chem. Soc.* **2019**, *141*, 17703-17712.

[14] R. Matsuda, R. Kitaura, S. Kitagawa, Y. Kubota, T. C. Kobayashi, S. Horike, M. Takata, *J. Am. Chem. Soc.* **2004**, *126*, 14063-14070.

[15] H. Li, F. Guo, J. Hu, C. Peng, H. Wang, H. Liu, J. Li, *J. Mate. Chem. A.* **2019**, *7*, 22353-22358.

[16] B. Li, C. Bai, S. Zhang, X. Zhao, Y. Li, L. Wang, K. Ding, X. Shu, S. Li, L. Ma, *J. Mate. Chem. A.* **2015**, *3*, 23788-23798.